

Waves in cell monolayer without proliferation: density determines cell velocity and wave celerity

S. Tlili, E. Gauquelin, B. Li, O. Cardoso, B. Ladoux, H. Delanoë-Ayari, F. Graner

arXiv:1610.05420v1 [physics.bio-ph] 18 Oct 2016

Waves in cell monolayer without proliferation: density determines cell velocity and wave celerity

Sham Tlili,^{1,2} Estelle Gauquelin,³ Brigitte Li,¹ Olivier Cardoso,¹ Benoît Ladoux,^{2,3} Hélène Delanoë-Ayari⁴ and François Graner¹

¹Laboratoire Matière et Systèmes Complexes, Université Denis Diderot - Paris 7, CNRS UMR 7057, Condorcet building, 10 rue Alice Domon et Léonie Duquet, F-75205 Paris Cedex 13, France;

²Mechanobiology Institute Department of Biological Sciences, National University of Singapore, 5A Engineering Drive 1 Singapore 117411;

³Institut Jacques Monod, Université Denis Diderot - Paris 7, CNRS UMR 7592, Buffon building, 15 rue Hélène Brion, F-75205 Paris Cedex 13, France;

⁴Univ. Lyon, Université Claude Bernard Lyon 1, CNRS UMR 5306, Institut Lumière Matière, Campus LyonTech - La Doua, Kastler building, 10 rue Ada Byron, F-69622 Villeurbanne Cedex, France

Abstract

Collective cell migration contributes to morphogenesis, wound healing or tumor metastasis. Culturing epithelial monolayers on a substrate is an *in vitro* configuration suitable to quantitatively characterize such tissue migration by measuring cell velocity, density and cell-substrate interaction force. Inhibiting cell division, we limit cell density increase and favor steady cell migration, while by using long narrow strips we stabilise the migrating front shape, so that we observe migration over a day or more. In the monolayer bulk, the cell velocity is a function of the cell density, namely it increases as a linear function of the cell radius. At least ten periods of propagating velocity waves are detected with a high signal-to-noise ratio, enabling for their quantitative spatio-temporal analysis. Cell density displays waves, in phase opposition with the velocity, as predicted by mass conservation; similarly, cell-substrate force appear to display small amplitude waves, in phase quadrature with respect to velocity, compatible with predictions for an elastic monolayer. The wave phase celerity is of order of ten micrometers per minute, i.e. ten times the monolayer migration velocity; wave celerity and frequency too decrease with cell density. We propose an experiment-inspired bottom-up biochemical model of these waves, where motility forces in the bulk of the monolayer are oriented by a dynamic pulling on cell-cell junctions. We find that parameters values close to the instability limit where waves appear yield predictions of wave characteristics close to experimentally observed values. These results lead to the determination of biomechanical parameters, strongly constrain possible theoretical models of waves propagation, and provide a new insight in the link between cell-level biomechanics or biochemistry and tissue-level collective cell migration.

Insert Received for publication Date and in final form Date.

Correspondence: mbitlil@nus.edu.sg, francois.graner@univ-paris-diderot.fr

Introduction

Collective migration of cells connected by cell-cell adhesion across large time scales and length scales occurs in numerous biological processes like embryogenesis (notably gastrulation), wound healing, regeneration or tumor metastasis (1–4). *In vitro* assemblies of cohesive cells are useful experimental model systems to study such mechanical behaviour of tissues (5–7). Within a reconstructed cell assembly, each individual cell retains its normal physiological behavior: it can grow, divide, die, migrate. The migration of cell monolayers has additional strategies over single cells to migrate since cell within the tissues interact with each other.

It is possible to constrain geometrically and reproducibly control the collective migration of a cell monolayer. Patterned substrate of adhesive strips enabled to investigate the tissue global response to active processes like cell migration (5, 8) or

cell division (9), and quantitatively test the impact of drugs such as blebbistatin (10). Two-dimensional (2D) systems such as Madin-Darby canine kidney (MDCK) cell monolayers facilitate experiments, simulations, theory and their mutual comparisons (11–16); 2D images are easier to obtain and analyze, enabling to extract physical quantities such as cell velocity, density, shape and deformation (13, 17).

When monolayers are grown on a substrate, the substrate acts as a source of external friction on cells (5, 8, 12, 18). If the substrate is deformable (made of soft gel or covered with pillars), it acts as a mechanical sensor for traction force microscopy to quantify forces exerted by cells on the substrate, which are the opposite of forces exerted by the substrate on the cells (19–21). Beside these external forces, internal forces within the monolayer include: cell growth and division (9); cell volume change (22); competition between the adhesion to the substrate, the intercellular adhesion and the cell contractility (23); cryptic lamellipodia extending from one cell below its neighbours (24).

The emergence of large-scale polarized movements within epithelial cell monolayers largely depends on external geometrical and mechanical constraints (8, 14, 17, 25). Microfluidic channel experiments have shown that the flow velocity of the front can be decomposed into a constant term of directed cell migration superimposed with a diffusion-like contribution that increases with density gradient (26). In the context of cell monolayers collectively spreading and invading a free space, highly motile leader cells can appear (27) and locally guide small organized cohorts of cells (11). Importantly, bulk cellular motions also display large-scale coordinated movements of cell clusters that can be seen by the emergence of large-scale polarization within the tissues (10, 28). Even though the appearance of such coordination is crucial to understand important biological functions, it remains poorly understood.

Serra-Picamal *et al.*, by confining cells on a strip then releasing the confinement on both sides, observed two periods of a propagating mechanical wave, indicating how stress mediates collective motion by propagating from the leading edge to the monolayer bulk (12). Similar wound healing experiments displayed a wave of coordinated migration, in which clusters of coordinately moving cells were formed away from the wound and disintegrated near the advancing front; this wave could be amplified by the hepatocyte growth factor / scatter factor (HGF/SF) (29). Confluent epithelial cells confined within circular domains exhibit collective low-frequency radial displacement modes as well as stochastic global rotation reversals (30, 31). Several phenomenological models have been developed to explain tissue-scale oscillations by invoking specific active mechanical ingredients, including cell-substrate traction force and cell contractile stress, and their feedbacks (12, 31–33). While oscillations at smaller scales are common in embryogenesis (cell size and minute period (34–37)) or myxobacteria swarms (a few cell sizes, 1 to 100 minutes period (38)), here in confluent monolayers the oscillation scale is that of a tissue size and of hours, reminiscent of somitogenesis (for review of models, see Ref. (39)). To improve our understanding, distinguish between the models, and constrain their parameters, more varied and reliable experimental data are required.

Here, by inhibiting cell division, we prevent cell density increase which would induce jamming, and by using long narrow strips we prevent front instability, so that we observe a steady, homogeneous collective migration over a day or more (Fig. 1, Fig. S1 and SI Movies 1-6). Propagating velocity waves are detected with an unprecedented signal-to-noise ratio, enabling for their quantitative analysis and comparison with modeling. We first average out the velocity field on a timescale larger than a few wave periods, to characterize the mean velocity profile. We find that in the monolayer bulk, the cell velocity depends only on the cell density, irrespectively of the distance to the migrating front, namely that it increases as a linear function of the cell effective radius. We then characterize more quantitatively the waves themselves, and find that their celerity and frequency decrease with cell density. Finally, we develop an experiment-inspired biochemical model of these waves, that provides a link between molecular mechanism at the single cell level and the emergence of multicellular coordinated responses within migrating monolayers.

Materials and methods

Cell monolayer

The micropattern of fibronectin is printed according to the following standard soft lithography technique, robust to small changes in the procedure. Patterned PDMS stamps prepared from silanized wafers are incubated for 45 min at 37°C or 60 min at room temperature with a solution of 50 $\mu\text{g/mL}$ of fibronectin (Sigma) and 25 $\mu\text{g/mL}$ of Cy3 conjugated fibronectin. A thin layer of PDMS (10 % of reticulating agent) is spin coated on a 35 mm plastic Petri dish and cured for 2 h at 80°C or overnight at 65°C. The Petri dish is exposed to UV for approximately 20 min in order to activate the PDMS surface. After incubation, stamps are dried and pressed on the UV activated PDMS surface in order to transfer fibronectin. A 2 % Pluronic F-127 (Sigma) solution is added to the Petri dish to chemically block the regions outside of the fibronectin pattern for 1 hour at room temperature. The Pluronic solution is removed after 1 hour and the Petri dish is rinsed 3 to 6 times with a PBS solution.

A batch has 3 to 6 strips, with the same initial MDCK cell density, possibly different widths from 200 to 1000 μm , and lengths up to 4 mm. Different batches correspond to different initial cell densities; each density is tested at least twice. The

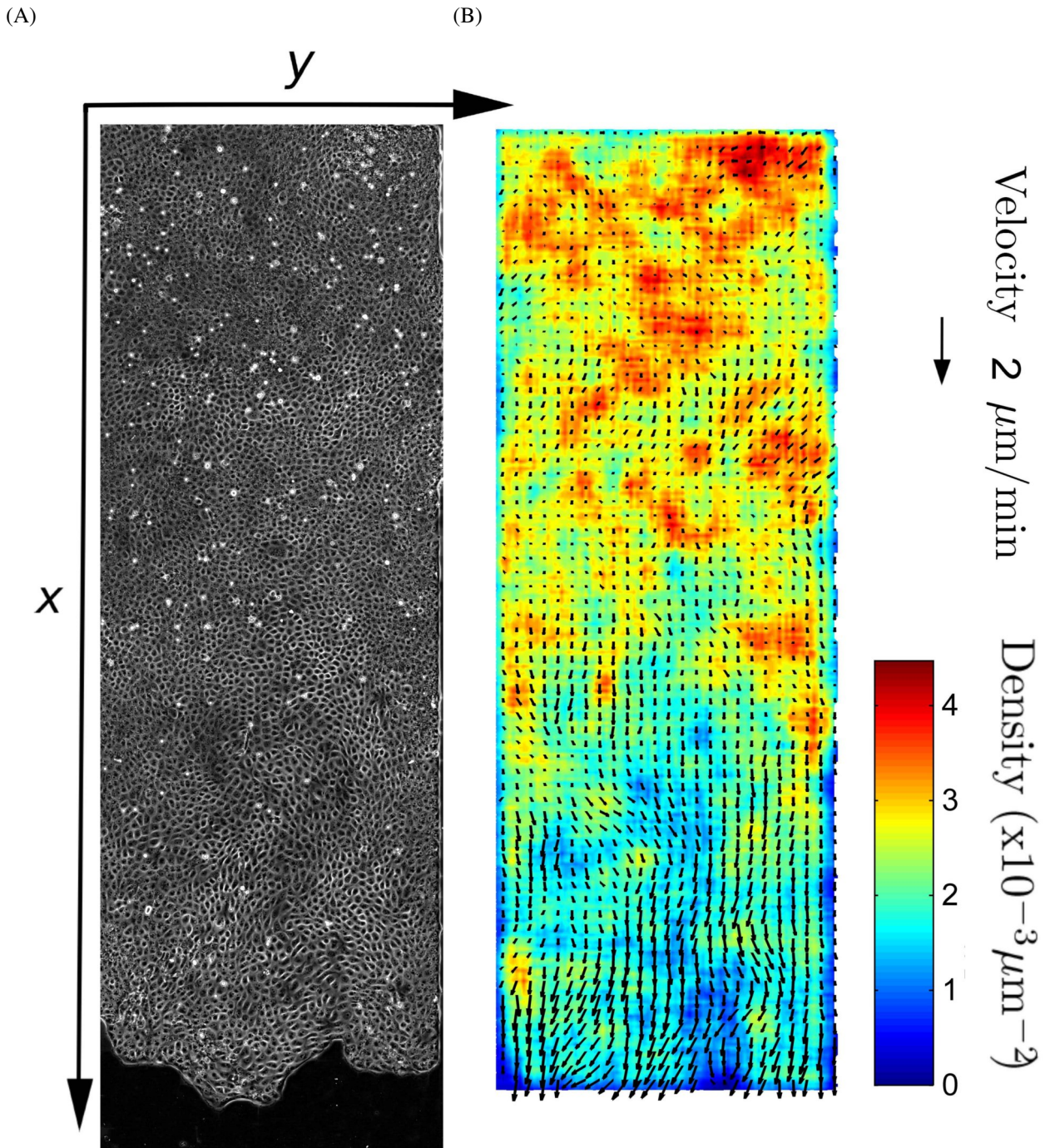


Figure 1: Monolayer of MDCK cells migrating within a straight strip with mitomycin C to prevent divisions (SI Movies 1-3). The monolayer is initially preconfined; at the beginning of the experiment, the confinement is released and the monolayer starts to expand along the adhesive strip towards empty space (direction of increasing x). (A) bright-field image of cell contours, strip total length 4 mm (most of it is visible here), width 1 mm. Picture taken at $t = 11$ h 30 after the first image (i.e. after around 16 h 30 of migration). (B) Corresponding 2D fields of velocity and density. Far from the front (top), the density is still close to its initial value and the velocity is still zero, while close to the front (bottom) the density has decreased and the velocity increased. Scale arrow: $2 \mu\text{m}/\text{min}$.

monolayer is first preconfined with a PDMS block ~ 8 mm in size, incubated in a 2 % Pluronic F-127 (Sigma) solution for 1 hour, then rinsed at least 6 times with a PBS solution. Suspended cells are deposited on the remaining accessible part, and allowed to attach for one to a few hours. Non-attached cells are rinsed, attached cells grow and divide until full confluence or overnight.

In order to decrease the division rate, 8 μL of a 0.5 mg/mL mitomycin C solution is added to 1 mL cell culture medium, and cells are incubated at 37°C for one hour. They are then abundantly rinsed with fresh 37°C medium. The confining PDMS block is removed. Some cells might detach, so the monolayer is rinsed again and left for a few hours. The monolayer starts to migrate along the whole adhesive strip, expanding towards empty adhesive surface. Division totally stops in the monolayer within ~ 5 hours.

Imaging

After these ~ 5 hours we take the first image of the movie and define it as $t = 0$. Live imaging of monolayers is performed in the Nikon BioStation IM, a compact cell incubator and monitoring system, with an air objective (CFI Plan Fluor 10X, Nikon). Bright-field and fluorescent imaging are used to observe respectively cell contours and cell nuclei. A stable cell line was created using Histone GFP (40) using the DreamFect Gold Transfection Reagent, Oz Biosciences. The interframe time interval is 5 min for 1 mm wide strips and 6 min for 0.2 mm wide strips on rigid substrates, and 12 min on soft substrates with force measurements.

Dead or extruded cells appear as bright spots which can be removed by manual image intensity thresholding. The contrast is adjusted separately on each color channel, and a blur with 2 pixel radius removes sharp intensity fluctuations. To obtain the whole view of the confined monolayer, up to 6 (for two 0.2 mm wide strips) or 20 (for 1 mm wide strips) microscope fields of view are merged using the Grid/Collection Stitching Plugin (41) implemented in ImageJ. We use the “unknown position” option for the first time frame to calculate automatically the overlap between images, which we use for all frames since images are stable.

Velocity and density

Velocity fields are computed in Matlab (The MathWorks, Inc., Natick, Massachusetts, United States), using the open source toolbox MATPIV *matpiv.m* (42) with the “singlepass” option. We use as box in (x, y) a square of side 32 pixels (20 μm) for 0.2 mm wide strips and 128 pixels (80 μm) for 1 mm wide strips, and box overlap is 50 % or 75 % for both widths. We measure the two-dimensional velocity field $\vec{v}(x, y, t)$ (Fig. 1B and Fig. S1A,C). We do not detect any statistically significant dependence of \vec{v} with y , even near the lateral sides of the strip. The y component of $\vec{v}(x, y, t)$ is lower at higher positions x where the average velocity is higher (Fig. S1C), indicating a more directed movement; we do not consider this component in what follows. The component of $\vec{v}(x, y, t)$ along the x axis, i.e. along the long axis of the strip, averaged over y , is the one-dimensional velocity field $V(x, t)$, which we study here.

To plot kymographs of $V(x, t)$, we remove noise using a gaussian blur of standard deviation 15 min and 30 μm (and a sliding window which is three times larger). We then separate scales, and decompose V into \bar{V} and $V - \bar{V}$, using a gaussian filter of standard deviation 50 min and 100 μm (again, with a sliding window which is three times larger). For large scale profiles \bar{V} , discrete measurements used for graphs are performed with an average on time t over 180 min and on space over 176 μm wide bins in the distance X to the moving front. Only significant data points are plotted, i.e. points with enough pixels in the 176 $\mu\text{m} \times 180$ min box (at least 150 pixels, out of a maximum of 612) and SD smaller than value. In particular, we entirely exclude the first box, where statistics are noisy due to the front.

Similarly, by identifying the nuclei (Fig. S1B), we measure the cell density $\rho(x, t)$, using boxes (x, y) of 20 $\mu\text{m} \times 20 \mu\text{m}$, then an average over y . The nuclei density can vary by a factor 10 within a given image. We first use a low blur radius, optimised for the highest nucleus density on the image. It yields a good detection for high density regions using *FastPeak-Find.m* but gives false positives (more than one local maxima per nucleus) for low density regions. When the distance between two maxima is smaller than a critical value (equal to a third of the average distance), we remove the less intense one. Manual checks on high, middle and low density regions have found that the measurement precision is better than 5 %. We have checked that tracking the cell nuclei yields more fluctuations than PIV for $\vec{v}(x, y, t)$ measurements, due to intra-cellular movements of nuclei (SI Movies 3-6), but yields same results as PIV for $V(x, t)$. Using the same filters as for V , we remove noise, decompose ρ into $\bar{\rho}$ and $\rho - \bar{\rho}$, and define discrete measurements of ρ versus X .

Wavelets

Kymographs are analysed using wavelet transform profilometry (WTP), a method inspired by 3D-fringe projection profilometry (43, 44). It involves a one-dimensional continuous wavelet transform with a phase estimation approach. It is reliable, easy to implement, and robust to noise. We choose a Morlet wavelet and the wavelet transform is computed using a FFT algorithm (which is equivalent to an analytic Morlet Wavelet) with a Matlab script (45).

For each kymograph line (i.e. for each fixed position x_i), the signal wavelet transform is computed at various time scales, ranging typically between 80 and 160 min, chosen in order to cover the full range of characteristic times of the observed oscillations. The wavelet transform returns a matrix of complex coefficients $A(x_i, t, s)$, defined as continuous wavelet coefficients where s represents the test times scales. Each coefficient provides a local measurement of the similarity between the signal and the wavelet at a scale s . For each point (x_i, t_j) of a given line i in the kymograph, only the coefficient $A_m(x_i, t_j)$ having the largest modulus with respect to the scale s is kept.

The argument of $A_m(x_i, t_j)$ provides the wrapped fringe phase $\phi_w(x_i, t_j)$. The phase $\phi_w(x_i, t_j)$ is unwrapped along time, and the local pulsation ω is deduced by differentiation with respect to time t . Independently, the phase $\phi_w(x_i, t_j)$ is unwrapped along space, and the local wave number k is deduced by differentiation with respect to space x .

Traction force microscopy

Traction force microscopy is performed according to a standard procedure (46) adapted here on PDMS substrates. The softest substrate stiffness modulus compatible with a good migration is 30 kPa; a rigid substrate (2 MPa) is used as a control. The fibronectin pattern and concentration are the same as on PDMS coated Petri dishes; the strip is not as straight but the lateral confinement is more efficient. The migration velocity is almost unchanged (it is slightly lower on softer substrates) and the same waves are observed.

Substrates were prepared from soft silicone gels (CY52-276A/B, Dow Corning) as described previously (47, 48) with some modifications. The two components (A:B) were mixed in a ratio of 5:6 (gel C in Table 1 of Ref. (49), Young modulus ~ 30 kPa), poured on a glass bottom Petri dish and cured at 80°C for 1 h. The substrates were silanized using a 10% (3-aminopropyl)triethoxysilane (Sigma) solution in ethanol for 10 min, rinsed three times with 100% ethanol and dried. They were incubated for 10 min with 200 nm carboxylated fluorescent beads (Invitrogen) diluted in Millipore water (1:500), washed and dried. Fibronectin patterns were first stamped on a thin membrane of polyvinyl alcohol (Sigma Aldrich) to then be transferred to the soft substrates (50). A 2% Pluronic solution was added for one hour to dissolve the membrane and to passivate the non-fibronectin coated areas. Thin PDMS blocks (~ 1 mm height) were prepared, silanized with (Tridecafluoro-1,1,2,2-tetrahydrooctyl)trichlorosilane and put silanized-face down on the soft substrates. Protocol is then the same than for experiments on PDMS substrate.

Cells and beads were imaged on a Nikon BioStation IM with a 10x objective. After imaging, cells were lysed using a 10% SDS solution and the “stress-free” image of the beads was obtained. Detection of the beads and their displacements were performed using the MATLAB function MatPIV (box size 9 pixels). The unconstrained stresses were computed using the ImageJ plugin FTTC (46). The bead density was large enough that the choice of the regularisation factor (here 10^{-9}) does not affect the results of force measurements.

To plot kymographs of $-F(x, t)$, we remove noise using a gaussian blur of standard deviation 5 min and 10 μm (and again a sliding window which is three times larger). We then decompose $-F$ into three scales using two gaussian filters: one of width 20 min, 40 μm , and one of width 100 min, 150 μm .

Results

Large scale profiles of velocity and density

By averaging over the direction y perpendicular to the stripes, we determine the one-dimensional cell velocity field $V(x, t)$ and cell density field $\rho(x, t)$. We first investigate their overall profiles \bar{V} , $\bar{\rho}$, obtained by large scale sliding average. Due to the spreading of cells close to the front, variations of velocity and density are visible (Fig. S2A,B). Note that far from the front, velocities are occasionally negative. We introduce the mean effective cell radius $R_{\text{mean}} = (\pi\bar{\rho})^{-1/2}$. Its typical range of variation is 8 to 15 μm ; for comparison, note that 4.8 μm corresponds to the nuclei being almost close packed, while 17 μm is the radius of a front cell at the limit of detaching from the monolayer.

With respect to the distance X to the moving front, different experiment batches display $\bar{V}(X)$ profiles which are qualitatively similar and quantitatively different (Fig. 2A). Accordingly, $R_{\text{mean}}(X)$ profiles from different experiment batches are qualitatively similar and quantitatively different (Fig. 2B). When eliminating the space variable X , points coming from

different experiment batches fall on the same curve: \bar{V} has a strong, negative correlation with $\bar{\rho}$ (14) (Fig. 2C, Fig. S2C). More precisely, \bar{V} increases linearly with R_{mean} (Fig. 2D), and this relation does not depend from the distance to the front (Fig. S2D). We have checked that this relation is unaffected when the sliding window size in time is doubled, and that there is no particular effect of the strip width on waves (Fig. S3A,B).

We also performed experiments under standard conditions (i.e. without mitomycin C, Fig. S3C,D). The range of observed densities increases twofold, while that of velocities decreases twofold. While the overall relation between $\bar{\rho}$ and \bar{V} seems qualitatively unaffected, dividing cells have a significantly larger \bar{V} at given $\bar{\rho}$, and a larger arrest density (Fig. 2C, Fig. S2C).

Propagating waves

We now turn to smaller scale variations. The cell velocity $V(x, t)$ displays waves. They are visible qualitatively on the movie where cells slow down and accelerate while waves propagate from the front backwards in the $-x$ direction (SI Movies 1-6). In the moving frame of average cell speed, these waves would appear as a periodic speed reversal. They are visible quantitatively on the space-time diagram or “kymograph” (Fig. S4A), and even more clearly on the velocity small scale variations $\tilde{V} = V - \bar{V}$ (Fig. 3A). The waves are reproducibly observed near the front, with a good signal-to-noise ratio over more than ten periods for a whole duration of observation of ~ 20 h.

First measurements are manual. They indicate that the waves have a period around two hours, their wavelength is around one mm. Their amplitude decrease with the distance to the front: waves are not apparent at the other end of the monolayer, where the density is as high as $5 \cdot 10^{-3} \mu\text{m}^{-2}$ and the velocity is as small as $0.1 \mu\text{m}/\text{min}$. Where they are visible, their amplitude is steady in time, and large: it represents a relative variation in local velocity which typically ranges from 15% to 30% (Fig. S4B), i.e. up to 60 % crest-to-crest. Their phase celerity (indicated by the slope of the phase crests) is of order of ten micrometers per minute, and with a sign opposed to that of the cell velocity (indicated by the slope of the front position). Their phase crests are visibly curved: this evidences that the celerity is larger near the front than in the middle of the monolayer.

Density small scale variations $\tilde{\rho} = \rho - \bar{\rho}$ are dominated by local heterogeneities, which are signatures of initial density fluctuations (cells do not significantly mix nor rearrange) over a typical length scale of $200 \mu\text{m}$. These fluctuations are advected at speed \bar{V} along with the monolayer itself: on the kymograph they appear as bars which, near the front, are almost parallel to the front; far from the front, they are closer to horizontal (Fig. 3B); in between, along the line drawn on Fig. 3C which has a slope of $0.31 \mu\text{m}/\text{min}$, we measure $\bar{V} = 0.33 \pm 0.02 \mu\text{m}/\text{min}$ (SD). In addition, and although they are less visible, it is clearly possible to distinguish waves on the density (Fig. 3B and Fig. S4C), which have the same period as the velocity waves and are in phase opposition with them (Fig. 3C,D). They have a small amplitude, with a relative variation ranging from 1% to 2 % (Fig. S4D), i.e. up to 4 % crest-to-crest.

Local wave characteristics

Since the wave characteristics are not homogeneous, we investigate them locally, in the regions where the cell velocity wave has a large enough signal-to-noise ratio (Fig. S4A). We use wavelet analysis to define, distinguish and measure $|\tilde{V}|$ and ϕ_V at each position x and time t , as follows: $|\tilde{V}|$ varies over large space and time scales (like \bar{V}), while ϕ_V encompasses the small space and time scale variations (Fig. S5A,B), and $\tilde{V} = \text{Re} \left(|\tilde{V}| \exp i\phi_V \right)$. Here $|\tilde{V}|$ tends to increase with \bar{V} (Fig. 4A), and accordingly decrease with $\bar{\rho}$.

The local phase ϕ of V in turn determines the local pulsation and wavenumber according to the sign convention $\omega = \partial\phi/\partial t$, $k = -\partial\phi/\partial x$ (here $k < 0$); then the local time period $T = 2\pi/\omega$ and wavelength $\lambda = 2\pi/|k|$. Both ω and k depend on space and time, due to the spatial variation of cell density (Fig. S2B), as reflected in the curvature of phase crests (Fig. 3A).

Finally, the wave phase celerity $c = \omega/k$ (here $c < 0$) is of order of minus ten times the cell velocity V ; c does decrease with mean effective cell radius R_{mean} (Fig. 4B) i.e. $|c|$ decreases with $\bar{\rho}$. We observe that ω increases when the density decreases (Fig. 4C). We do not observe any correlation of ω , k or c with X .

Again using wavelet analysis we define and measure $|\tilde{\rho}|$ and ϕ_ρ : $\tilde{\rho} = \text{Re} \left(|\tilde{\rho}| \exp i\phi_\rho \right)$ (Fig. S5C,D). The kymograph of ϕ_ρ shows that the wavelets detect the signal which physically corresponds to the wave velocity, and filter out irrelevant variations (Fig. 4D).

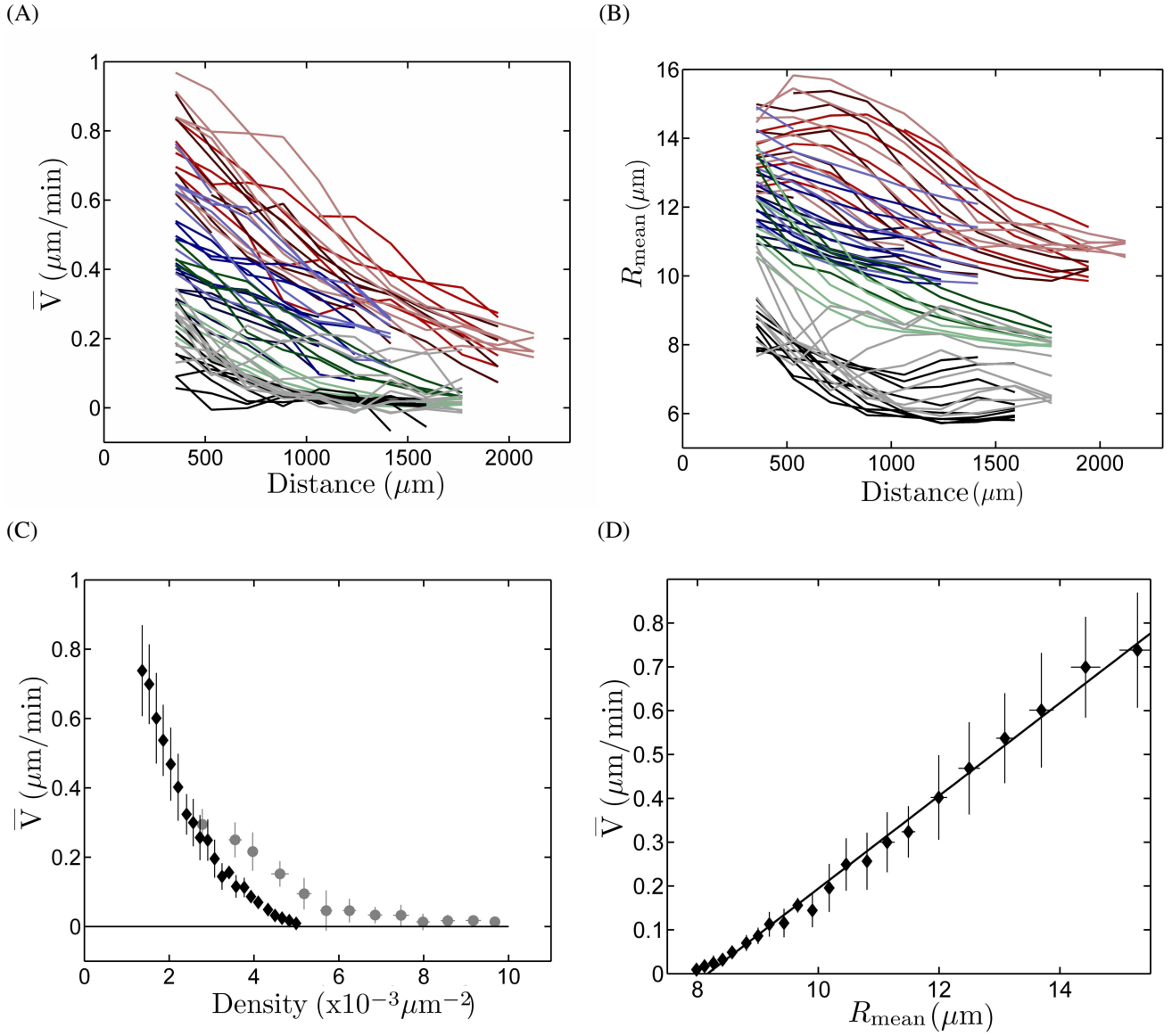


Figure 2: Large scale profiles. (A,B) Large-scale average (\pm SD) of cell velocity \bar{V} (A) and mean effective cell radius $R_{\text{mean}} = (\pi\bar{\rho})^{-1/2}$ (B), plotted vs distance X to migrating front. Each color marks a different batch, with red, blue, green in order of increasing initial density. For a given color (i.e. batch), each shade marks a different strip. For a given shade (i.e. strip), each line is a different time, every 180 min. For a given line (i.e. time), each data point is the average in a box of $176 \mu\text{m} \times 180 \text{ min}$. Grey levels are the same, for control experiments under standard conditions (i.e. without mitomycin C). (C,D) Binned plots; the horizontal and vertical bars are the standard deviation (SD) within each bin. (C) Black: same data as in (A,B), binned and plotted as cell velocity \bar{V} vs cell density $\bar{\rho}$. Grey: control experiments under standard conditions (i.e. without mitomycin C). (D) Same data as in (A,B), binned and plotted as cell velocity \bar{V} vs mean effective cell radius R_{mean} , with a linear fit $\bar{V} = 0.106 R_{\text{mean}} - 0.864$ ($R=0.9931$).

Modeling

We propose to use continuum mechanics (51) to describe the cell monolayer migrating on a substrate with a one-dimensional model. We first propose some phenomenological description to perform experimental tests. Then, we introduce a possible model to explain the existence of waves, based on biochemistry-biomechanics coupling, which we link with experiments to extract relevant parameters.

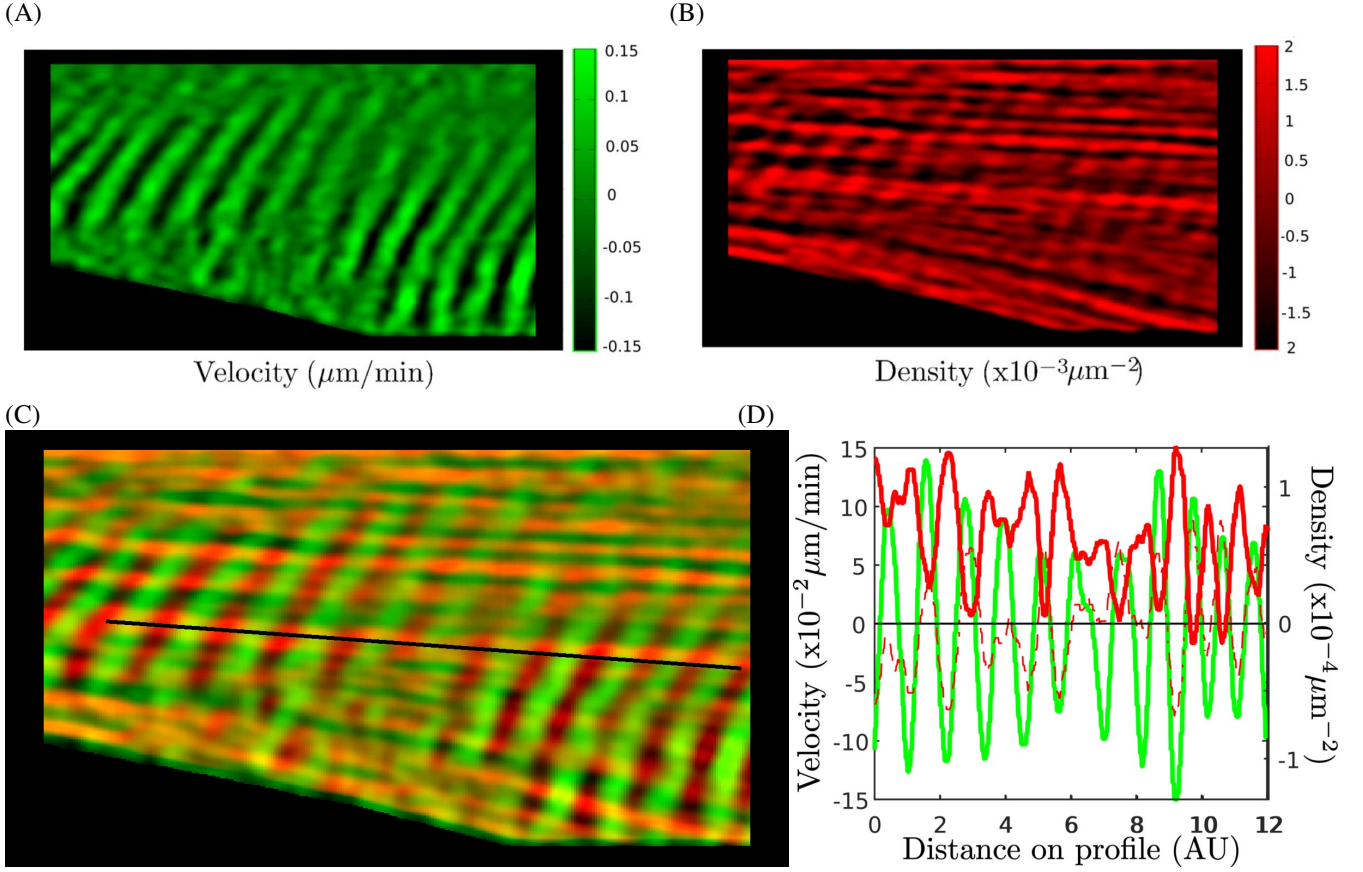


Figure 3: Propagating waves. (A-C) Space-time diagram (kymograph) of small scale variations in cell velocity, $\tilde{V} = V - \bar{V}$ (A), in density, $\tilde{\rho} = \rho - \bar{\rho}$ (B), and merge, (C). Space x is from top (0 mm) to bottom (3 mm), time t from left (0 h) to right (25 h), and the bottom-left region is the bare substrate in front of the monolayer. Color code \tilde{V} from $-0.15 \mu\text{m}/\text{min}$ (black) to $0.15 \mu\text{m}/\text{min}$ (green), $\tilde{\rho}$ from $-1.3 \times 10^{-3} \mu\text{m}^{-2}$ (black) to $1.3 \times 10^{-3} \mu\text{m}^{-2}$ (red). The line is manually drawn. (D) Plot of \tilde{V} (green) and $\tilde{\rho}$ (red) along the line manually drawn in (C). Inverting the sign of $\tilde{\rho}$ (red dashes) evidences their phase opposition, which agrees with Eq. (2).

Phenomenology and orders of magnitude

In absence of cell division, the mass conservation or cell number conservation is expressed as

$$\frac{\partial \rho}{\partial t} + \frac{\partial(\rho V)}{\partial x} = 0 \quad (1)$$

Linearizing Eq. (1) for small wave amplitude (i.e. neglecting the $\tilde{\rho}\tilde{V}$ term), and introducing $c = \omega/k$, yields

$$\tilde{\rho}(c - \bar{V}) = \bar{\rho}\tilde{V}. \quad (2)$$

Since the order of magnitude of c is minus ten times that of V , Eq. (2) predicts that $\tilde{\rho}$ is in phase opposition with \tilde{V} , and that $\tilde{\rho}/\bar{\rho}$ is minus a tenth of \tilde{V}/\bar{V} . This explains why the oscillations on the density are barely visible in Fig. 3B. By measuring the velocity and density wave characteristics at several points, we observe a local variability (see an example on Fig. S5). We take advantage of this variability to check over a wide range that Eq. (2) is compatible with the observed oscillation amplitude, at least at small amplitude, Fig. S6A (Eq. (2) is checked with 10% precision). Phases even check Eq. (2) with 1% precision (Fig. 3D, Fig. 4D, Fig. S6B).

The dissipation could contribute to stress in series or in parallel with elasticity (51). The dissipative contribution in series with the elasticity results in a monolayer viscoelastic time τ (of order of 3 to 5 hours (52, 53)), which does not modify the value of the stress, and only contributes to regularize the wave instability, see section “Equations of the model”. The characteristic time of waves (wave appearance and/or wave period) is 1-2 hour and thus smaller than τ . Conversely, we neglect the

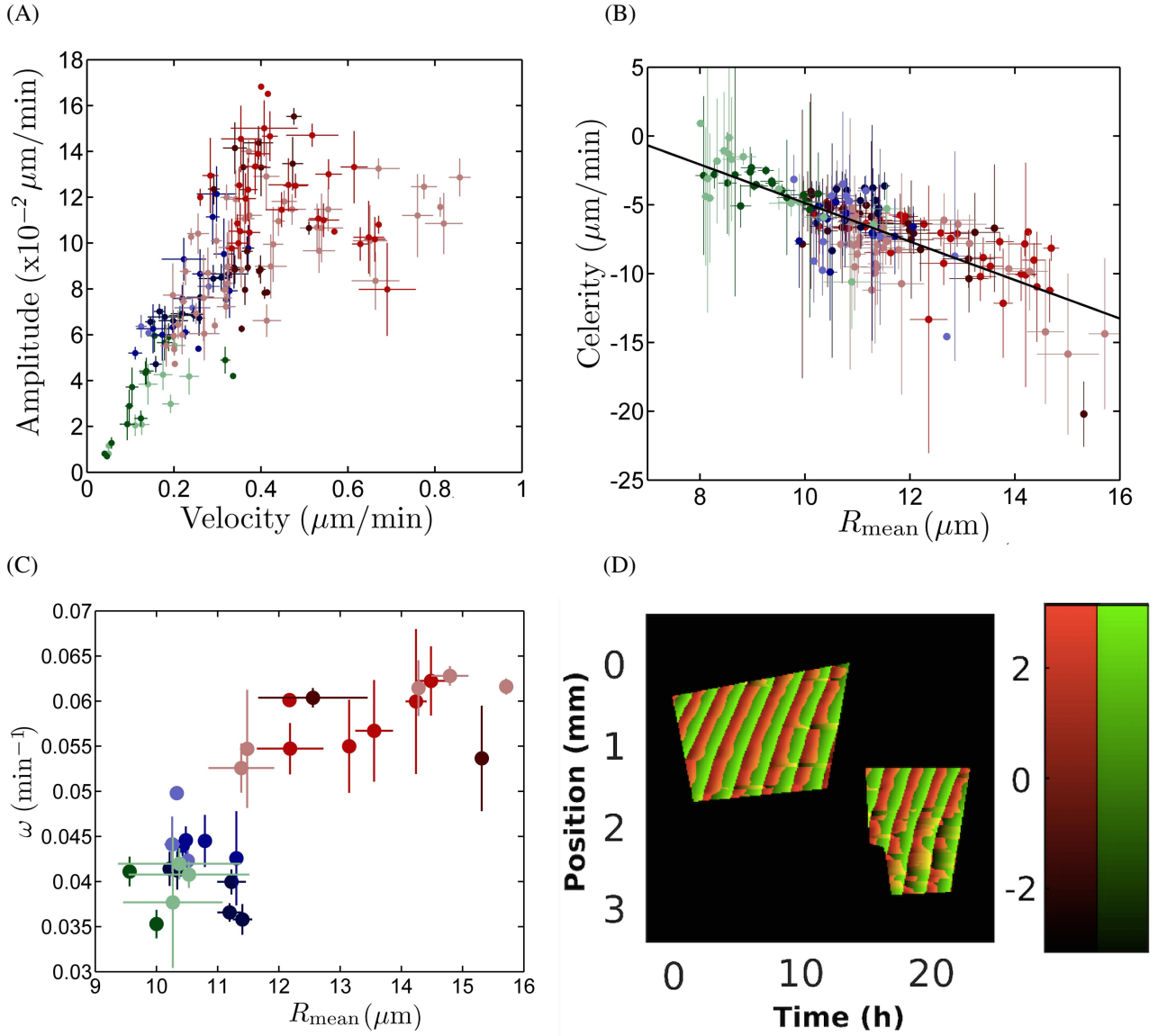


Figure 4: Local wave characteristics, determined by wavelet analysis in the region of interest (Fig. S4A). (A) Amplitude $|\tilde{V}|$ (\pm SD) of velocity waves, versus average velocity \bar{V} ; $N = 156$ data points. (B) Wave phase celerity c versus mean effective cell radius R_{mean} , with a linear fit $c = 9.2 - 1.4 R_{\text{mean}}$ ($R=0.59$); $N = 155$ data points (one outlier has been removed). (C) Pulsation ω vs R_{mean} : each point results from the spatial average \pm std both of ω and of R_{mean} , over their respective profiles vs distance X to the migrating front, at a same time. In (A,B,C) same color code as Fig. 2A,B. (D) Merged kymographs of phases: ϕ_ρ from $-\pi$ (black) to π (red), and ϕ_V from $-\pi$ (black) to π (green), data from Fig. S5B,D.

viscosity contribution in parallel with the elasticity (31). In fact, with upper estimates of the 3D cell viscosity η of order of 10^2 Pa s (52, 54), we use the values of the friction coefficient $\zeta \sim 10^9$ N m⁻³ s (15, 31) and a wavenumber $k \sim 10^4$ rad m⁻¹, and we obtain that the modulus of the internal viscous force $\eta k |\tilde{V}|$ is at least thousand times smaller than that of the typical external friction force, $\zeta \bar{V}$.

The stress is dominated by its elastic contribution,

$$\sigma = Ge \quad (3)$$

Here e is the elastic deformation, which in linear elasticity (near the front) writes $e \approx 1 - \rho/\rho_e$; ρ_e is the elastic reference density reached at the limit of confluence, of order of 10^{-3} μm⁻² (Fig. 2C); G is the elastic modulus. Typical values of G

are in the range $10^2 - 10^3$ Pa, obtained for single cell (55), by micro-indentation (56, 57) or on a monolayer (48) (stretching a suspended monolayer, including cell-cell junctions, yields a much larger value $\sim 2 \cdot 10^4$ Pa (13)).

The force equilibrium of the monolayer (integrated along the normal to the substrate) relates the external force per unit area F , exerted by the substrate on the cell monolayer, and the internal forces, namely the divergence of stress, as

$$\frac{\partial(h\sigma)}{\partial x} + F = 0, \quad (4)$$

where σ is the 1D stress (equivalent to the 3D stress component along xx) averaged over the monolayer thickness h . Within this 1D analysis of the experiment, Eq. (4) relates F and σ without any ambiguity nor hypothesis on the monolayer rheology (12, 58). Assuming the cell volume incompressibility,

$$\frac{h}{\rho} = \frac{\bar{h}}{\bar{\rho}} = \text{cst} \quad (5)$$

achieves to determine F .

If F undergoes waves too, we define $\tilde{F} = F - \bar{F}$, while \bar{F} can vanish if all cells migrate as a whole. Using again a complex notation, Eqs. (2)-(5) yield

$$\tilde{F} = -ikG\tilde{h} = -ikG\bar{h}\frac{\tilde{V}}{c - \bar{V}} = -i\frac{|k|G\bar{h}}{|c| + \bar{V}}\tilde{V} \quad (6)$$

This predicts that \tilde{F} is in quadrature with respect to \tilde{V} ; physically, this quadrature comes from the fact that \tilde{F} is in quadrature with stress and deformation, which themselves are in phase due to our assumption of an elastic behaviour (31). With the value $\bar{h} \sim 10 \mu\text{m}$ (Supp. Fig. S7 of Ref. (12), see also Ref. (33)), the amplitude $|\tilde{F}|/G$ is estimated as less than a hundredth of $|\tilde{V}|/\bar{V}$.

A traction force experiment measures the local forces per unit area exerted by cells on the substrate (Fig. S7A), with components at different scales (Fig. S7B-D). Small scales include dipolar fluctuations and noise, due to intra-cell and inter-cell variability; these forwards and backwards forces fluctuate in the range of plus or minus several 10^2 Pa over length scales of one to a few cells (10 to $100 \mu\text{m}$). The intermediate scales reflect the forces exerted by the cell monolayer on the substrate, coarse-grained at a scale smaller than the speed correlation length in MDCK cell monolayers (10); these coarse-grained forces are linked with the divergence of the monolayer stress. The large scales reflect density variations.

The force waves $-\tilde{F}$ predicted by Eq. (6) should exist at intermediate scales (1 mm), in the range 10 to 100 Pa ; we thus expect them to be dominated by the small scale signal. In fact, in most of our experiments, due to the noise level, no force wave is detectable. However, in a few experiments (such as in Fig. S7C), the intermediate scales appear to display oscillations. Their amplitude would be close to our detection limit, $\sim 10 \text{ Pa}$ (Fig. S7E-F), compatible with Eq. (6) for a value $G = 10^3 \text{ Pa}$, which is a reasonable order of magnitude for the elastic modulus. Their phase would have a quadrature compatible with Eq. (6) ($-F$ is in advance over V).

Model for wave appearance

Several models have been proposed to explain the instability which gives rise to waves by invoking one of various active cell ingredients, within the constraints raised by symmetry considerations (12, 31–33, 59) (see also Ref. (60), in a different context). The force per unit area exerted by the substrate on the monolayer is sometimes written as the sum of active and friction contributions, $F = f_a p - \zeta V$ (15). Here p is the one-dimensional equivalent of the cell polarization: it is a number between -1 and 1, indicating in which direction the cell exerts an active force, and at which proportion of its maximum possible active cell force f_a (of order of 300 Pa (5)), which decreases with ρ (8, 9, 14). It is convenient to introduce $V_a = f_a/\zeta$, which corresponds to an active migration velocity, and write

$$\frac{F}{\zeta} = V_a p - V. \quad (7)$$

Combining Eqs. (1), (3)-(5) and (7) yields the strain evolution equation,

$$\frac{\partial e}{\partial t} + V \frac{\partial e}{\partial x} = \frac{\partial^2 (De)}{\partial x^2} + \frac{\partial (V_a p)}{\partial x} \quad (8)$$

If h was fixed, Eq. (8) would be a diffusion equation, with an effective diffusion coefficient $D = Gh/\zeta$; D increases with monolayer stiffness and decreases with friction. In principle, there might be an instability if the heterogeneity of the active

term V_{ap} overcomes the stabilising diffusion term. A heterogeneity in migration force might create a heterogeneity in velocity, affecting in turn the stress, which would feed back on the force. The question is how this feedback could become positive.

A recent paper by Das *et al.* (61) has revealed how motility forces can coordinate far from the migrating front inside the monolayer. When the cell is at rest, the protein Merlin (a tumor suppressor) is localized at the cell-cell junctions. This junctional Merlin inhibits the formation of cryptic lamellipodia. On the other hand, when cell-cell junctions experience a stretching stress, Merlin is relocated to the cytoplasm. Due to the decrease in junctional Merlin, the Rac pathway becomes activated, within a delay time of a few tens of minutes. Then, within a much smaller delay, Rac activates the generation of cell polarization and lamellipodia, responsible for the migrating forces (61). In addition, when a cell migrates and is polarized, its front end has more cytoplasmic and less junctional Merlin than its rear end (T. Das, personal communication, 2016).

Starting from the mechanism suggested by Fig. 8a of Ref. (61) for the polarization of the front cell, we suggest a mechanism by which strain induces migration propagation through a feedback loop (Fig. S8). Moreover, in absence of experimental data, we speculate a reciprocal mechanism by which the absence of strain induces, again through a feedback loop, the propagation of the migration arrest (Fig. S9).

Equations of the model

To implement this double mechanism and relate it quantitatively with our experimental observations, we propose a semi-quantitative model. It couples a cell's mechanical response, its polarization, and its asymmetry in Merlin concentrations. Its level of detail is suited to the available amount of experimental data. In particular, we neglect: non-linearities, viscosity, as well as the large scale variation of \bar{V} and ρ over the whole strip length scale. These simplifying hypotheses can easily be relaxed if required could easily be refined if future experiments add new details.

The total amount of Merlin contained in the cell exists in two forms (Fig. 5A). We note J the fraction of the junctional Merlin molecules, attached to the cell-cell junction, and C the fraction of the cytoplasmic Merlin molecules, free to diffuse within the cell. To account for the front-rear asymmetry, we distinguish the fractions at the front end of the cell, J^f and C^f , and at the rear end of the cell, J^r and C^r , with $J^f + C^f + J^r + C^r = 1$. More precisely, since we describe the monolayer within continuum mechanics, the four values J^f , C^f , J^r and C^r are fractions of concentrations coarse-grained on scales larger than the cell size.

The mechanics is described by Eqs. (3)-(5), (7)-(8). We focus on the stability of a steady state where all cell migrate in the same direction, $\bar{V} > 0$, and are positively polarized, $\bar{p} > 0$. The symmetric steady state, with \bar{V} and \bar{p} negative, is irrelevant here (unlike in symmetric migration experiments (12)). The third steady state, $\bar{V} = 0$, exists initially, but ceases to be stable when the confinement is removed, and is also irrelevant here.

The biochemistry is described by kinetic parameters, noted r , which are reaction rates or inverse of characteristic times. Cytoplasmic concentration differences $C^f - C^r$ tend to disappear at a rate r_D , equal to the cytoplasmic diffusion coefficient D_{cyto} (typically of order of $200 \mu\text{m}^2\text{min}^{-1}$ for a protein of the size of Merlin, 70 kD (62)) divided by the square cell length, i.e. $r_D \sim \bar{\rho} D_{\text{cyto}} 10^{-2} \text{ s}^{-1}$. Changing this value, even to extremes ($r_D \rightarrow 0$, no diffusion, or $r_D \rightarrow \infty$, homogeneous concentration) affects only quantitatively, but not qualitatively, the results presented below.

Junctional Merlin becomes cytoplasmic at a rate r_e which depends on the tissue strain e . From Fig. 3e of (61) we estimate that $r_e^1/r_e^0 \approx 120$. Thus $r_e^0 \ll r_e^1$. Fig. 3i of Ref. (61) indicates that for a strain $e = 25\%$, half of junctional Merlin relocates to cytoplasm in ~ 10 min. This yields $r_e^1 \sim 1/(3 \text{ min}) \sim 55 \cdot 10^{-4} \text{ s}^{-1}$. Hence $r_e^0 \sim 1.5 \cdot 10^{-4} \text{ s}^{-1}$. For simplicity we interpolate linearly and write $r_e = r_e^0 + r_e^1 e$.

Conversely, cytoplasmic Merlin becomes junctional at a rate r_p , modulated by the cell polarization p : it is increased by the activity of Rac1, i.e. r_p is larger at the front end. There is no available experimental data to determine the value of r_p , but we can determine bounds as follows. Supp. Fig. S3 of Ref. (61) provides an image of junctional and cytoplasmic Merlin in unpolarized cells without strain. Visually, it appears that around junctional and cytoplasmic Merlin account respectively for around 90% and 10% of the total. This yields an order of magnitude for the ratio r_p/r_e^0 in absence of polarization: $r_p/r_e^0 \sim 9$. Hence for a polarized cell, defining the ratios $\alpha^f = r_p^f/r_e^0$ at the front end and $\alpha^r = r_p^r/r_e^0$ at the rear end, we estimate bounds $\alpha^f < 9 < \alpha^r$.

In turn, the cytoplasmic Merlin activates the Rac1 pathway and lamellipodia formation with a delay time, which globally lumps the kinetics of several reactions. The inverse of this characteristic time is r_R , and can be estimated using Fig. 7h of Ref. (61): $r_R \sim 8 \pm 3 \cdot 10^{-4} \text{ s}^{-1}$ (SEM).

The biochemical rates defined above (r_D , $r_e = r_e^0 + r_e^1 e$, r_p^f , r_p^r , r_R) can be used to write the evolution equations of polarization p and the four Merlin fractions (J^f , J^r , C^f , C^r). We take into account the advection by using the notation

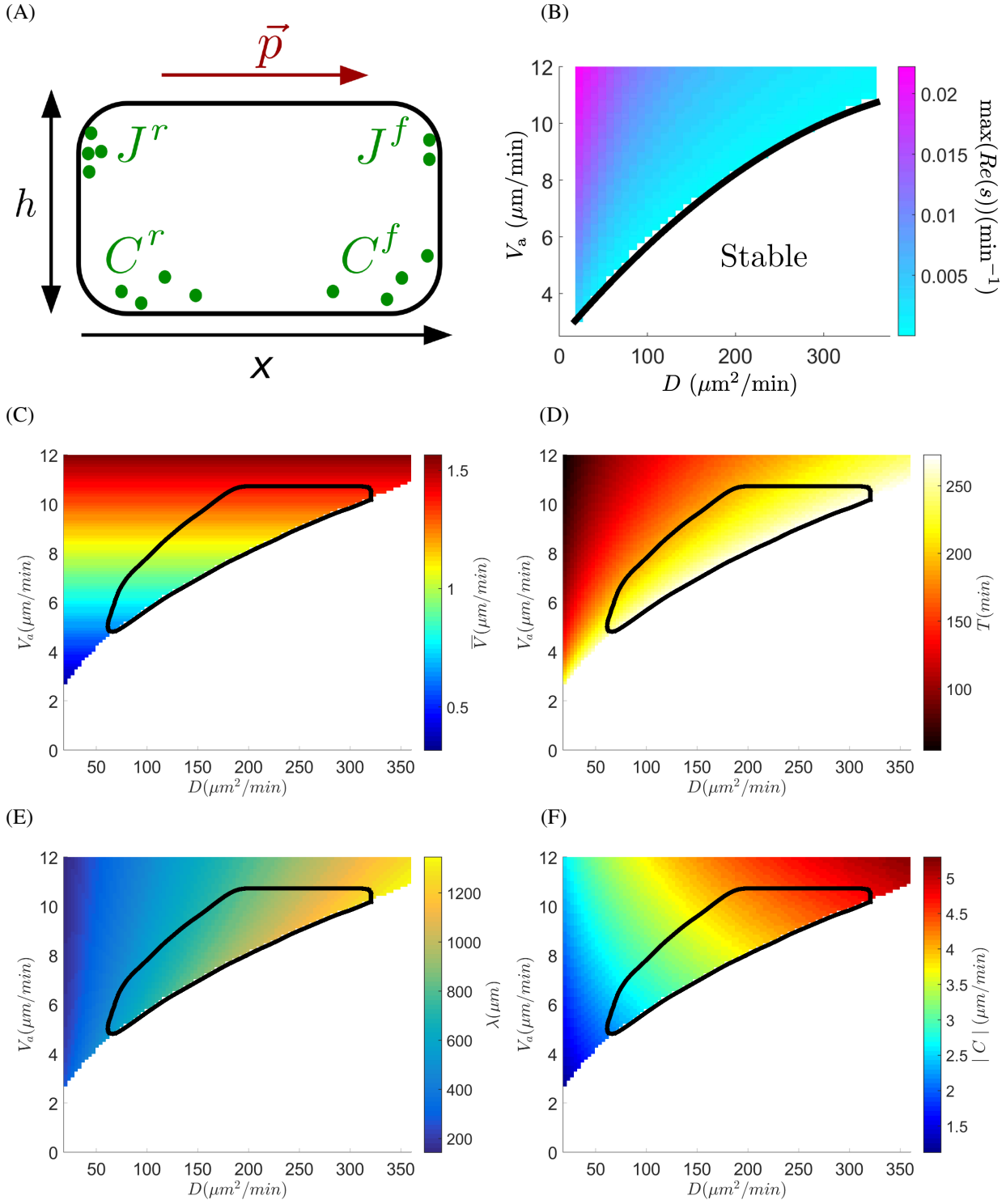


Figure 5: Model of wave appearance. (A) Notations. (B) Instability threshold: value of active migration velocity V_a above which waves appear, versus diffusion coefficient D . The solid line is a quadratic fit to the instability threshold ($V_a = 3.73 \cdot 10^{-5} D^2 + 3.66 \cdot 10^{-2} D + 2.39$). The linear growth rate is indicated by the color code. (C-F) Model predictions, versus parameters D and V_a (the highlighted region indicates the constraints by experimental measurements) for values of wave characteristics: (C) \bar{V} , (D) T , (E) λ , (F) $|c|$.

$d/dt = \partial/\partial t + V\partial/\partial x$. We translate the above ingredients into evolution equations written as simply as possible:

$$\frac{dp}{dt} = r_R (J^r - J^f - p) \quad (9)$$

$$\frac{dJ^f}{dt} = -r_e(e)J^f + r_p^f C^f = -(r_e^0 + r_e^1 e) J^f + \alpha^f r_e^0 C^f \quad (10)$$

$$\frac{dJ^r}{dt} = -(r_e^0 + r_e^1 e) J^r + \alpha^r r_e^0 C^r \quad (11)$$

$$\frac{dC^f}{dt} = -\frac{\partial J^f}{\partial t} + r_D (C^r - C^f) \quad (12)$$

$$\frac{dC^r}{dt} = -\frac{\partial J^r}{\partial t} - r_D (C^r - C^f) \quad (13)$$

If the boundary conditions were periodic (e.g. on a ring), eqs. (4), (7), (9)-(13) would admit a continuous family of steady, homogeneous solutions ($\partial_t = \partial_x = 0$), parametrized by the density $\bar{\rho}$ (or equivalently by the strain \bar{e}) where all cells migrate and are polarized: $\bar{C}^f = \bar{C}^r = \bar{C} = (2 + r_e^0(\alpha^f + \alpha^r)/(r_e^0 + r_e^1 e))^{-1}$, while $\bar{J}^f = \alpha^f \bar{C}$, $\bar{J}^r = \alpha^r \bar{C}$, $\bar{p} = (\alpha^r - \alpha^f) \bar{C}$, $\bar{V} = V_a (\alpha^r - \alpha^f) \bar{C}$, and $\bar{F} = 0$.

We can take into account the monolayer viscoelastic time τ , by distinguishing the total deformation rate \dot{e} from the elastic deformation rate de/dt , with $\dot{e} = de/dt - e/\tau$. This adds to the r.h.s. of Eq. (8) a term $-e/\tau$. In what follows, we solve the equations with $\tau = 5$ h, which regularizes the wave parameters. We check that taking the limit $\tau \rightarrow \infty$ modifies the wave period and wavelength only close to the instability limit (where they diverge), and conversely taking τ shorter than the hour (eg $\tau = 30$ min, comparable to the delay time of Merlin) suppresses the instability.

We look at small perturbations (of the steady, homogeneous state) proportional to $\exp(st - ikx)$, where s and k are real numbers. Taking as independent variables \tilde{e} , \tilde{p} , \tilde{J}^f , \tilde{J}^r , and \tilde{C}^f , we obtain a set of five linear equations, which Jacobian is:

$$\mathcal{J} = \begin{pmatrix} s - ik\bar{V} + Dk^2 + \tau^{-1} & ikV_a & 0 & 0 & 0 \\ 0 & 1 + \frac{s-ik\bar{V}}{r_R} & 1 & -1 & 0 \\ \frac{\alpha^f r_e^1}{\alpha^f + \alpha^r + 2(r_e^0 + r_e^1 e)/r_e^0} & 0 & s - ik\bar{V} + r_e^0 + r_e^1 e & 0 & -r_p^f \\ \frac{\alpha^r r_e^1}{\alpha^f + \alpha^r + 2(r_e^0 + r_e^1 e)/r_e^0} & 0 & r_p^r & s - ik\bar{V} + r_e^0 + r_e^1 e + r_p^r & r_p^r \\ 0 & 0 & s + r_D & r_D & s - ik\bar{V} + 2r_D \end{pmatrix} \quad (14)$$

The determinant of \mathcal{J} has 5 roots, which depend on parameter values and of k . We find them numerically by solving for instance the case $\bar{e} = 0$, which is relevant in the region close to the front where the waves are most visible, and which is the stable state when τ is finite. In addition, calculations near $\bar{e} = 0$ are simple, as terms of order \bar{e} in \mathcal{J} are suppressed, and as terms due to variations of h are second order and thus negligible.

We look for a root which has a strictly positive real part, $\text{Re}(s) > 0$, and a non zero imaginary part, $\text{Im}(s) \neq 0$. Depending on the parameter values, there are two possible situations (Fig. 5B). Either no such root exists for any k , then the steady, homogeneous solution is stable. Or there exists a range of k with one such root, and the steady, homogeneous solution is unstable. In the latter situation, a propagating wave appears; the mode k which develops more quickly is that for which $\text{Re}(s)$ is maximum, i.e. $d\text{Re}(s)/dk = 0$ (until the amplitude increases enough to reach the non-linear regime). Its imaginary part $\text{Im}(s)$ is the pulsation ω of this mode.

Results of the model

The phase diagram mostly depends on D and V_a . The numerical resolution of the equations determines when V_a is strong enough to overcome D (Fig. 5B). For a reasonable set of biochemical parameters, we find a maximum instability rate for $D^{\max} = 120 \mu\text{m}^2/\text{min}$ and $V_a^{\max} = 7 \mu\text{m}/\text{min}$, corresponding to $\lambda^{\max} \sim 600 \mu\text{m}$, $T^{\max} \sim 250$ min, $c^{\max} \sim 3 \mu\text{m}/\text{min}$.

More generally, the model also predicts how \bar{V} and wave characteristics such as T , λ , and $|c|$ depend on model parameters V_a and D (Fig. 5C-F). Based on the typical range we measure for these quantities (see for instance Fig. S5), we delimitate the intersection of the regions corresponding to \bar{V} in range 0 to $1.4 \mu\text{m}/\text{min}$, T in range 100 to 300 min, λ in range 500 to $2000 \mu\text{m}$, $|c| \geq 2 \mu\text{m}/\text{min}$. These constraints on the model parameters (region highlighted in Fig. 5C-F) enable to infer their values: we find $V_a = 8.6 \pm 1.5 \mu\text{m}/\text{min}$ and $D = 180 \pm 67 \mu\text{m}^2/\text{min}$ (SEM). These values, in turn, yield $G = 500 \pm 185$ Pa and $f_a = 143 \pm 25$ Pa, which are in the range expected from the literature, and compatible with Fig. S7F.

We have plotted Fig. 5B by using moderate values of the ratios α (namely $\alpha^f = r_p^f/r_e^0 = 9$ and $\alpha^r = r_p^r/r_e^0 = 12$). Changing these ratios widely, while obeying $\alpha^f \leq 9 \leq \alpha^r$, allows to explore their effect on wave characteristics (Fig. S10). The values of α^f , α^r do not significantly affect the instability limit shown in Fig. 5B. In principle, using Fig. S10, it should be possible to infer the values of α^f , α^r in addition to that of D and V_a .

Discussion

We observe that in migrating monolayers, the cell velocity increases linearly with the mean effective cell radius, suggesting that the traction force too is proportional to the cell radius.

Our experimental measurements of propagating velocity wave characteristics, and their dependence in the model parameters should strongly constrain analytical models or numerical simulations in the future. We have already checked their agreement between our observations and predictions arising from phenomenological equations.

The wave phase celerity too depends on density, and is an order of magnitude larger than the monolayer migration velocity (compare Fig. 4B with Fig. 2D or Fig. S2D). Backwards-propagating waves are generated while velocity decreases with density, which might belong to a generic instability mechanism (originally discussed in the context of car traffic (63)). Density waves are in phase opposition with velocity waves, and have a smaller amplitude. Force waves have an even smaller amplitude, at the limit of detection; they seem in phase with stress and deformation, in quadrature with velocity.

For a given experiment, although the density is spatially heterogeneous, the velocity waves have a pulsation ω which is spatially homogeneous. It might arise from the fact that the most developed mode temporally forces the instability over the whole monolayer, resulting in a heterogeneous wavenumber k . Now, comparing experiments at different densities, we observe that ω increases when the density decreases (Fig. 4C). This is compatible with the model: we expect that when ρ decreases, V_a increases significantly while D is not much affected; this is represented on Fig. 5D by a vertical upwards trajectory, where the period T decreases and ω increases.

The most visible effect of divisions is to steadily increase the density, which contributes to jamming and decreases the migration velocity; however, at given density, the divisions themselves contribute to increase the monolayer movement and the front velocity. In addition, divisions increase the noise in velocity; more regions have a negative velocity (Fig. S3C,D). With divisions, the velocity waves are either inexistant, less visible or non propagating (overdamped), possibly due to long range ordering in the velocity field (64).

Our observations are compatible with a large-scale polarized activity induced for instance by activity of Merlin protein, as recently shown experimentally (61). The cells at the front of the migrating monolayers are known to exert large traction forces (48, 65) that can induce the build-up of a large intercellular stress and in turn, a polarization of the following cell by a relocalization of Merlin from the cell-cell junctions to the cytoplasm. The iteration of such processes may lead to large scale polarization within the tissue.

Inspired by published observations and by our own, we propose here a simple bottom-up biochemical model where motility forces in the bulk of the monolayer are oriented by a dynamic pulling on cell-cell junctions. We perform a linear stability analysis, neglecting the monolayer internal viscosity as well as the large scale density and thickness variations which would lead only to second-order corrections. With reasonable parameters values, we find propagating waves with a frequency and a wavenumber of the same order than the experimental values. The phase diagram of spontaneous instability shows that the observed waves appear close to the instability limit (Fig. 5B). This could explain why waves had been difficult to detect in the past (12, 29) (see also the Supp. Figs. S2, S5 of Ref. (31)), as parameters can change depending on cell size or substrate coating. In the future, non-linear analysis of the model could determine the wave amplitudes and compare them with measurements (Fig. 4A).

Our model makes predictions which can be tested experimentally. First, simultaneous independant measurements of ζ , G , h and f_a would determine D and V_a , which can be confronted with the values we have inferred. Second, live imaging of the spatial distribution of motility markers like Rac or Rho, and even possibly of Merlin, could be correlated with cell polarization, deformation and migration forces. Such study should shed light on the role of long-range information propagation mediated by mechanical stress, during both *in vitro* cell migration and *in vivo* embryogenesis.

Author contributions

S.T., B.La., H.D.-A., F.G. designed the research; S.T., E.G., performed experiments; S.T., E.G., B.Li, O.C., analysed experiments; S.T., B.Li, F.G. developed the model; S.T., B.Li, H.D.-A., F.G. wrote the manuscript; all authors discussed the results and the manuscript.

Acknowledgments

We warmly thank T. Das, F. Gallet, Y. Jiang, P. Marcq, U. Schwarz for discussions.

References

- [1] Keller, R., 2002. Shaping the vertebrate body plan by polarized embryonic cell movements. *Science* 298:1950–4.
- [2] Friedl, P., Y. Hegerfeldt, and M. Tusch, 2004. Collective cell migration in morphogenesis and cancer. *Int. J. Devel. Biol.* 48:441–9.
- [3] Friedl, P., and D. Gilmour, 2009. Collective cell migration in morphogenesis, regeneration and cancer. *Nat. Rev. Mol. Cell Biol.* 10:445–57.
- [4] Arboleda-Estudillo, Y., M. Krieg, J. Stühmer, N. Licata, D. Muller, and C. Heisenberg, 2010. Movement directionality in collective migration of germ layer progenitors. *Curr. Biol.* 20:161–9.
- [5] Trepap, X., M. R. Wasserman, T. E. Angelini, E. Millet, D. A. Weitz, J. P. Butler, and J. J. Fredberg, 2009. Physical forces during collective cell migration. *Nat. Phys.* 5:426–430.
- [6] du Roure, O., A. Saez, A. Buguin, R. H. Austin, P. Chavrier, P. Silberzan, and B. Ladoux, 2005. Force mapping in epithelial cell migration. *Proc. Natl. Acad. Sci. U.S.A.* 102:2390–5.
- [7] Cohen, D., W. J. Nelson, and M. M. Mahabiz, 2014. Galvanotactic control of collective cell migration in epithelial monolayers. *Nat. Mater.* 13:409–17.
- [8] Angelini, T. E., E. Hannezo, X. Trepap, J. J. Fredberg, and D. A. Weitz, 2010. Cell migration driven by cooperative substrate deformation patterns. *Phys. Rev. Lett.* 104:168104/1–4.
- [9] Puliafito, A., L. Hufnagel, P. Neveu, S. Streichan, A. Sigal, D. K. Fygenson, and B. I. Shraiman, 2012. Collective and single cell behavior in epithelial contact inhibition. *Proc. Natl. Acad. Sci. U.S.A.* 109:739–44.
- [10] Vedula, S. R. K., M. C. Leong, T. L. Lai, P. Hersen, A. J. Kabla, C. T. Lim, and B. Ladoux, 2012. Emerging modes of collective cell migration induced by geometrical constraints. *Proc. Natl. Acad. Sci. U.S.A.* 109:12974–79.
- [11] Refay, M., L. Petitjean, S. Coscoy, E. Grasland-Mongrain, F. Amblard, A. Buguin, and P. Silberzan, 2011. Orientation and polarity in collectively migrating cell structures: statics and dynamics. *Biophys. J.* 100:2566–75.
- [12] Serra-Picamal, X., V. Conte, R. Vincent, E. Anon, D. T. Tambe, E. Bazellieres, J. P. Butler, J. J. Fredberg, and X. Trepap, 2012. Mechanical waves during tissue expansion. *Nat. Phys.* 8:628–34.
- [13] Harris, A. R., L. Peter, J. Bellis, B. Baum, A. J. Kabla, and G. T. Charras, 2012. Characterizing the mechanics of cultured cell monolayers. *Proc. Natl. Acad. Sci. U.S.A.* 109:16449–54.
- [14] Doxzen, K., S. R. K. Vedula, M. C. Leong, H. Hirata, N. S. Gov, A. J. Kabla, B. Ladoux, and C. T. Lim, 2013. Guidance of collective cell migration by substrate geometry. *Integrative Biol.* 5:1026–35.
- [15] Cochet-Escartin, O., J. Ranft, P. Silberzan, and P. Marcq, 2014. Border forces and friction control epithelial closure dynamics. *Biophys. J.* 106:65.
- [16] Albert, P. J., and U. S. Schwarz, 2016. Dynamics of cell ensembles on adhesive micropatterns: bridging the gap between single cell spreading and collective cell migration. *PLoS Comput. Biol.* 12:e1004863/1–34.
- [17] Tambe, D. T., C. Corey Hardin, T. E. Angelini, K. Rajendran, C. Y. Park, X. Serra-Picamal, E. H. Zhou, M. H. Zaman, J. P. Butler, D. A. Weitz, J. J. Fredberg, and X. Trepap, 2011. Collective cell guidance by cooperative intercellular forces. *Nat. Mater.* 10:469–75.
- [18] Saez, A., E. Anon, M. Ghibaudo, O. du Roure, J.-M. di Meglio, P. Hersen, P. Silberzan, A. Buguin, and B. Ladoux, 2010. Traction forces exerted by epithelial cell sheets. *J. Phys. Cond. Mat.* 22:194119/1–9.
- [19] Dembo, M., T. Oliver, A. Ishihara, and K. Jacobson, 1996. Imaging the traction stresses exerted by locomoting cells with the elastic substratum method. *Biophys. J.* 70:2008–22.
- [20] Schwarz, U. S., N. Balaban, D. Riveline, A. Bershadsky, B. Geiger, and S. Safran, 2002. Calculation of forces at focal adhesions from elastic substrate data: the effect of localized force and the need for regularization. *Biophys. J.* 83:1380–1394.
- [21] Plotnikov, S., B. Sabass, U. Schwarz, and C. Waterman, 2015. High resolution traction force microscopy. *Methods Cell Biol.* 123:367–94.
- [22] Zehnder, S. M., M. Suaris, M. M. Bellaire, and T. E. Angelini, 2015. Cell Volume Fluctuations in MDCK Monolayers. *Biophys. J.* 108:247–50.
- [23] Hannezo, E., J. Prost, and J.-F. Joanny, 2014. Theory of epithelial sheet morphology in three dimensions. *Proc. Natl. Acad. Sci. U.S.A.* 111:27–32.
- [24] Farooqui, R., and G. Fenteany, 2005. Multiple rows of cells behind an epithelial wound edge extend cryptic lamellipodia to collectively drive cell-sheet movement. *J. Cell Sci.* 118:51–63.
- [25] Ng, M. R., A. Besser, G. Danuser, and J. S. Brugge, 2012. Substrate stiffness regulates cadherin-dependent collective migration through myosin-II contractility. *J. Cell Biol.* 199:545–63.
- [26] Marel, A.-K., M. Zorn, C. Klingner, R. Wedlich-Söldner, E. Frey, and J. O. Rädler, 2014. Flow and diffusion in channel-guided cell migration. *Biophys. J.* 107:1054–64.
- [27] Ladoux, B., R.-M. Mège, and X. Trepap, 2016. Front-rear polarization by mechanical cues: from single cells to tissues. *Trends Cell Biol.* 26:420–33.
- [28] Pujade, M., E. Grasland-Mongrain, A. Hertzog, J. Jouanneau, P. Chavrier, B. Ladoux, A. Buguin, and P. Silberzan, 2007. Collective

- migration of an epithelial monolayer in response to a model wound. *Proc. Natl. Acad. Sci. U.S.A.* 104:15988–93.
- [29] Zaritsky, A., D. Kaplan, I. Hecht, S. Natan, L. Wolf, N. S. Gov, E. Ben-Jacob, and I. Tsarfay, 2014. Propagating Waves of Directionality and Coordination Orchestrate Collective Cell Migration. *PLoS Comput. Biol.* 10:e1003747.
 - [30] Deforet, M., V. Hakim, H. Yevick, G. Duclos, and P. Silberzan, 2014. Emergence of collective modes and tri-dimensional structures from epithelial confinement. *Nat. Commun.* 5:3747.
 - [31] Notbohm, J., S. Banerjee, K. J. C. Utuje, B. Gweon, H. Jang, Y. Park, J. Shin, J. P. Butler, J. J. Fredberg, and M. C. Marchetti, 2016. Cellular contraction and polarization drive collective cellular motion. *Biophys. J.* 110:2729–38.
 - [32] Blanch Mercader, C., 2015. Mechanical instabilities and dynamics of living matter: From single-cell motility to collective cell migration. Ph.D. thesis, Universitat de Barcelona.
 - [33] Banerjee, S., K. J. Utuje, and M. C. Marchetti, 2015. Propagating stress waves during epithelial expansion. *Phys. Rev. Lett.* 114:228101.
 - [34] Solon, J., A. Kaya-Copur, J. Colombelli, and D. Brunner, 2009. Pulsed forces timed by a ratchet-like mechanism drive directed tissue movement during dorsal closure. *Cell* 137:1331–42.
 - [35] Martin, A. C., M. Gelbart, R. Fernandez-Gonzalez, M. Kaschube, and E. F. Wieschaus, 2010. Integration of contractile forces during tissue invagination. *J. Cell Biol.* 188:735–49.
 - [36] Maître, J.-L., R. Niwayama, H. Turlier, F. Nédélec, and T. Hiiragi, 2015. Pulsatile cell-autonomous contractility drives compaction in the mouse embryo. *Nat. Cell Biol.* 17:849–55.
 - [37] Maître, J.-L., H. Turlier, R. Illukkumbura, B. Eismann, R. Niwayama, F. Nédélec, and T. Hiiragi, 2016. Asymmetric division of contractile domains couples cell positioning and fate specification. *Nature* 536:344–8.
 - [38] Wu, Y., A. D. Kaiser, Y. Jiang, and M. S. Alber, 2009. Periodic reversal of direction allows Myxobacteria to swarm. *Proc. Natl. Acad. Sci. U.S.A.* 106:1222–7.
 - [39] Oates, A. C., N. Gorfinkel, M. González-Gaitán, and C.-P. Heisenberg, 2009. Quantitative approaches in developmental biology. *Nat. Gen.* 10:517–30.
 - [40] Fukunaga, Y., H. Liu, M. Shimizu, S. Komiya, M. Kawasuji, and A. Nagafuchi, 2005. Defining the roles of beta-catenin and plakoglobin in cell-cell adhesion: isolation of beta-catenin/plakoglobin-deficient F9 cells. *Cell Struct. Funct.* 30:25–34.
 - [41] Preibisch, S., S. Saalfeld, and T. Tomancak, 2009. Globally optimal stitching of tiled 3D microscopic image acquisitions. *Bioinformatics* 25:1463–1465.
 - [42] Sveen, J. K., 2004. An introduction to MatPIV v. 1.6.1. eprint series, Dept. of Math. University of Oslo NO. 2 ISSN 0809-4403.
 - [43] Gdeisat, M. A., D. R. Burton, and M. J. Lalor, 2006. Spatial carrier fringe pattern demodulation by use of a two-dimensional continuous wavelet transform. *Appl. Optics* 45:8722–8732.
 - [44] Gdeisat, M. A., A. Abid, D. R. Burton, M. J. Lalor, F. Lilley, C. Moore, and M. Qudeisat, 2009. Spatial and temporal carrier fringe pattern demodulation using the one-dimensional continuous wavelet transform: Recent progress, challenges, and suggested developments. *Optics Lasers Engineer.* 47:1348–1361.
 - [45] 2016. MATLAB cwtft - MathWorks, <http://fr.mathworks.com/help/wavelet/ref/cwtft.html>.
 - [46] Martiel, J.-L., A. Leal, L. Kurzawa, M. Baland, I. Wang, T. Vignaud, Q. Tseng, and M. Théry, 2015. Measurement of cell traction forces with ImageJ. *Methods Cell Biol.* 125:269–87.
 - [47] Mertz, A., Y. Che, S. Banerjee, J. Goldstein, K. Rosowski, S. Revilla, C. Niessen, M. Marchetti, E. Dufresne, and V. Horsley, 2013. Cadherin-based intercellular adhesions organize epithelial cell-matrix traction forces. *Proc. Natl. Acad. Sci. U.S.A.* 110:842–7.
 - [48] Vedula, S., H. Hirata, M. Nai, A. Brugués, Y. Toyama, X. Trepas, C. Lim, and B. Ladoux, 2014. Epithelial bridges maintain tissue integrity during collective cell migration. *Nat. Mater.* 13:87–96.
 - [49] Kenry, M. C. Leong, M. H. Nai, F. C. Cheong, and C. T. Lim, 2015. Viscoelastic effects of silicone gels at the micro- and nanoscale. *Procedia IUTAM* 12:20–30.
 - [50] Yu, H., S. Xiong, C. Y. Tay, W. S. Leong, and L. P. Tan, 2012. A novel and simple microcontact printing technique for tacky, soft substrates and/or complex surfaces in soft tissue engineering. *Acta Biomater.* 8:1267–72.
 - [51] Tlili, S., C. Gay, F. Graner, P. Marcq, F. Molino, and P. Saramito, 2015. Colloquium: Mechanical formalisms for tissue dynamics. *Eur. Phys. J. E* 38:33/1–31.
 - [52] Guevorkian, K., M.-J. Colbert, M. Durth, S. Dufour, and F. Brochard-Wyart, 2010. Aspiration of biological viscoelastic drops. *Phys. Rev. Lett.* 104:218101/1–4.
 - [53] Vincent, R., E. Bazellieres, C. Pérez-González, M. Uroz, X. Serra-Picamal, and X. Trepas, 2015. Active tensile modulus of an epithelial monolayer. *Phys. Rev. Lett.* 115:248103/1–5.
 - [54] Stirbat, T. V., A. Mgharbel, S. Bodennec, K. Ferri, H. C. Mertani, J.-P. Rieu, and H. Delanoë-Ayari, 2013. Fine tuning of tissues viscosity and surface tension through contractility suggests a new role for α -Catenin. *PLoS One* 8:e52554.
 - [55] Moeendarbary, E., L. Valon, M. Fritzsche, A. R. Harris, D. A. Moulding, A. J. Thrasher, E. Stride, L. Mahadevan, and G. T. Charras, 2013. The cytoplasm of living cells behaves as a poroelastic material. *Nat. Mater.* 12:253–61.
 - [56] Harris, A., and G. Charras, 2011. Experimental validation of atomic force microscopy-based cell elasticity measurements. *Nanotechnology* 22:345102.
 - [57] Pietuch, A., B. R. Brückner, T. Fine, I. Mey, and A. Janshoff, 2013. Elastic properties of cells in the context of confluent cell monolayers: impact of tension and surface area regulation. *Soft Matter* 9:11490–502.
 - [58] Nier, V., S. Jain, C. T. Lim, S. Ishihara, B. Ladoux, and P. Marcq, 2016. Inference of internal stress in a cell monolayer. *Biophys. J.*

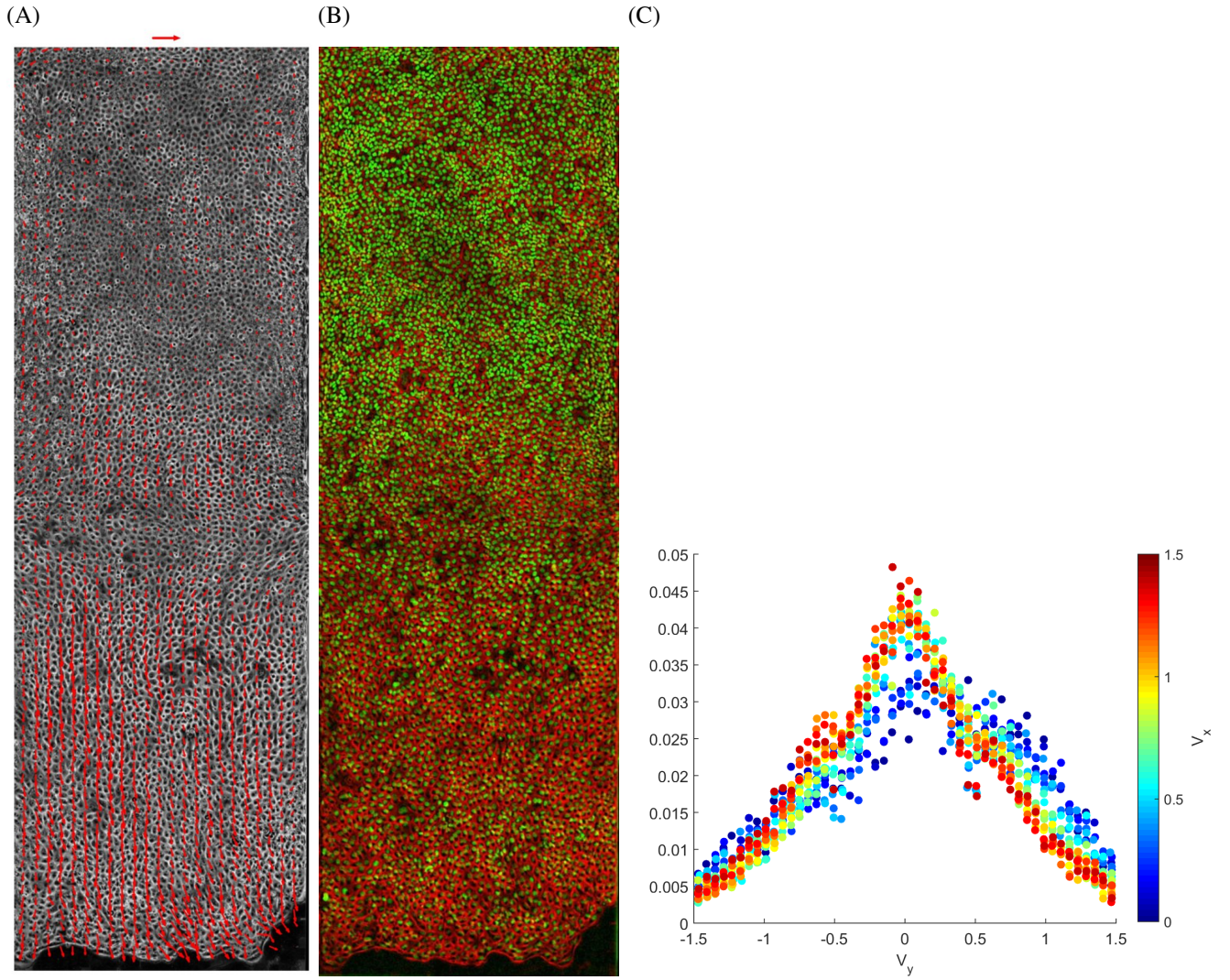
110:1625–35.

- [59] Recho, P., J. Ranft, and P. Marcq, 2016. One-dimensional collective migration of a proliferating cell monolayer. Soft Matter 12:2381–91.
- [60] Marcq, P., 2014. Spatio-temporal dynamics of an active, polar, viscoelastic ring. Eur. Phys. J. E 37:29.
- [61] Das, T., K. Safferling, S. Rausch, N. Grabe, H. Boehmand, and J. P. Spatz, 2015. A molecular mechanotransduction pathway regulates collective migration of epithelial cells. Nat. Cell Biol. 17:276–87.
- [62] Nenninger, A., G. Mastroianni, and C. Mullineaux, 2010. Size dependence of protein diffusion in the cytoplasm of *Escherichia coli*. J. Bacteriol. 192:4535–40.
- [63] Lighthill, M. J., and G. B. Whitham, 1955. On kinematic waves. II. A theory of traffic flow on long crowded roads. Proc. R. Soc. Lond. A 229:317–45.
- [64] Rossen, N., J. Tarp, J. Mathiesen, M. Jensen, and L. Oddershede, 2014. Long-range ordered vorticity patterns in living tissue induced by cell division. Nat. Commun. 5:5720.
- [65] Reffay, M., M. Parrini, O. Cochet-Escartin, B. Ladoux, A. Buguin, S. Coscoy, F. Amblard, J. Camonis, and P. Silberzan, 2014. Interplay of RhoA and mechanical forces in collective cell migration driven by leader cells. Nat. Cell Biol. 16:217–23.

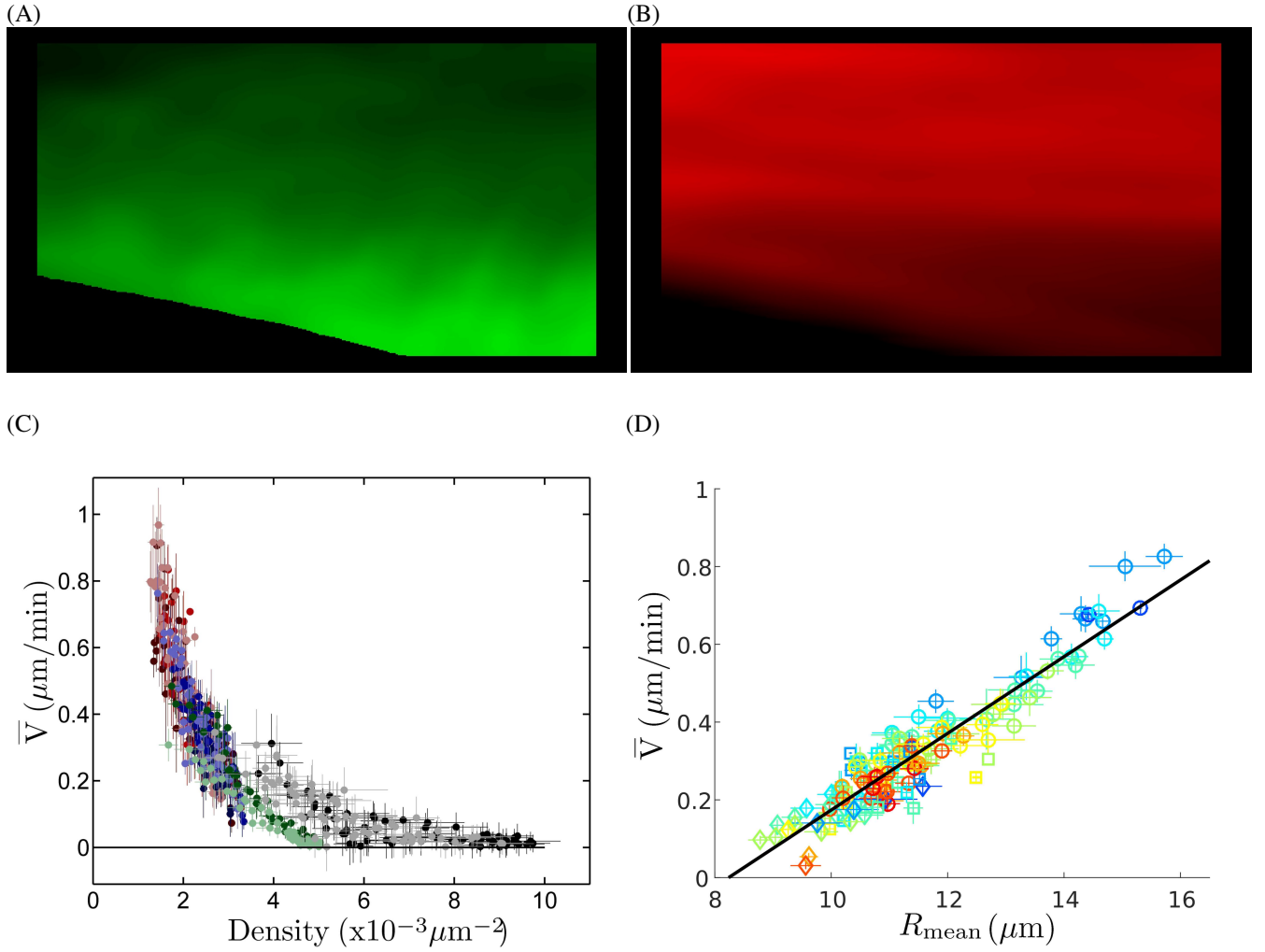
Waves in cell monolayer without proliferation: density determines cell velocity and wave celerity

S. Tlili, E. Gauquelin, B. Li, O. Cardoso, B. Ladoux, H. Delanoë-Ayari, F. Graner

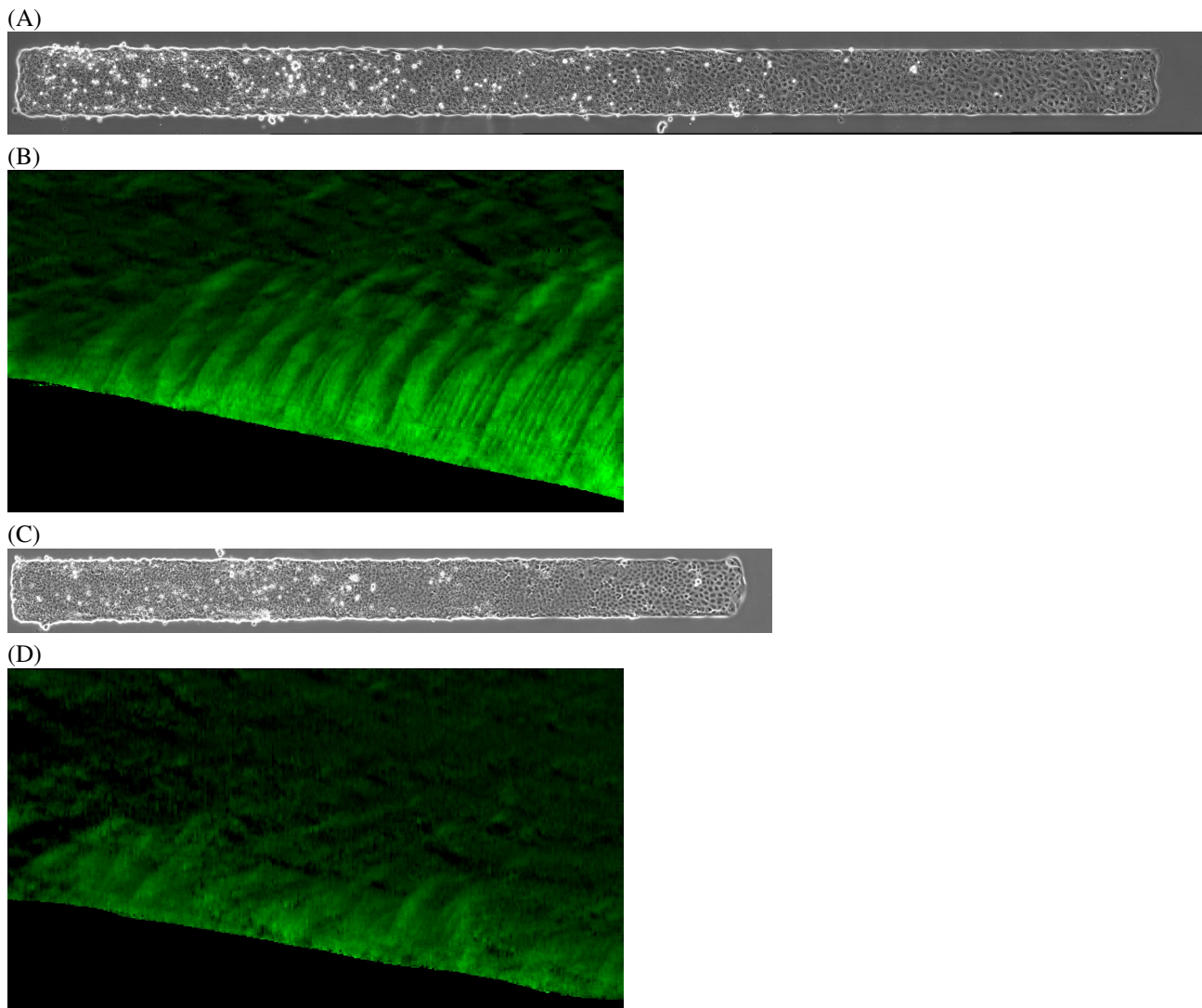
Supporting Information



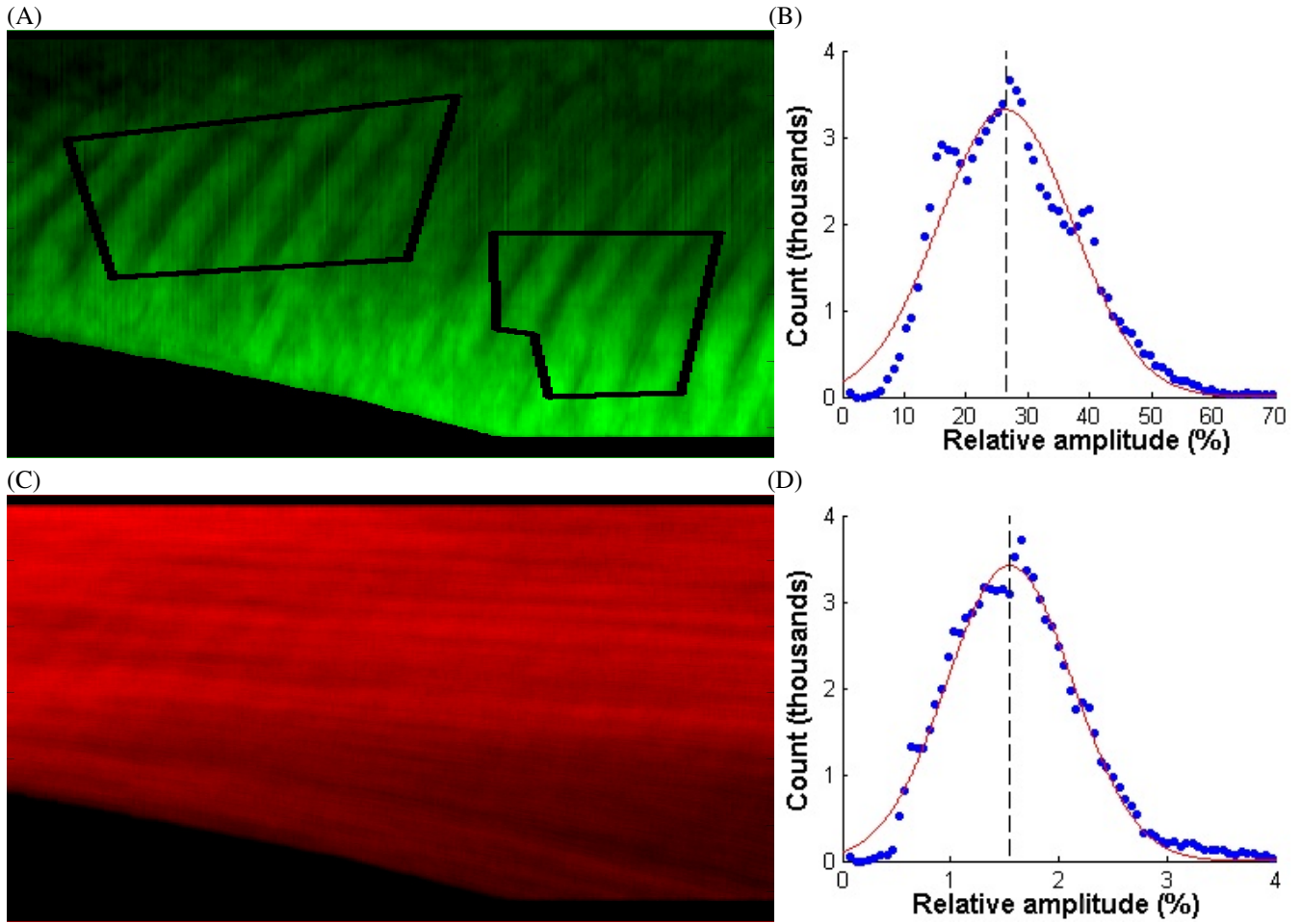
Supporting Figure S1. Cell velocity and density. (A) Instantaneous velocity field $\vec{v}(x, y, t)$ superimposed on cell contours, at $t = 15$ h after the first image (i.e. after around 20 h of migration). Scale arrow: $2 \mu\text{m}/\text{min}$. (B) Corresponding picture of nuclei labeled with histone GFP evidence the large scale cell density variation; they can be detected for cell density measurement, and tracked for cell velocity validation. Cell contours appear in red. (C) Distributions of y component of velocity field $\vec{v}(x, y, t)$, while its x component is indicated by the color code.



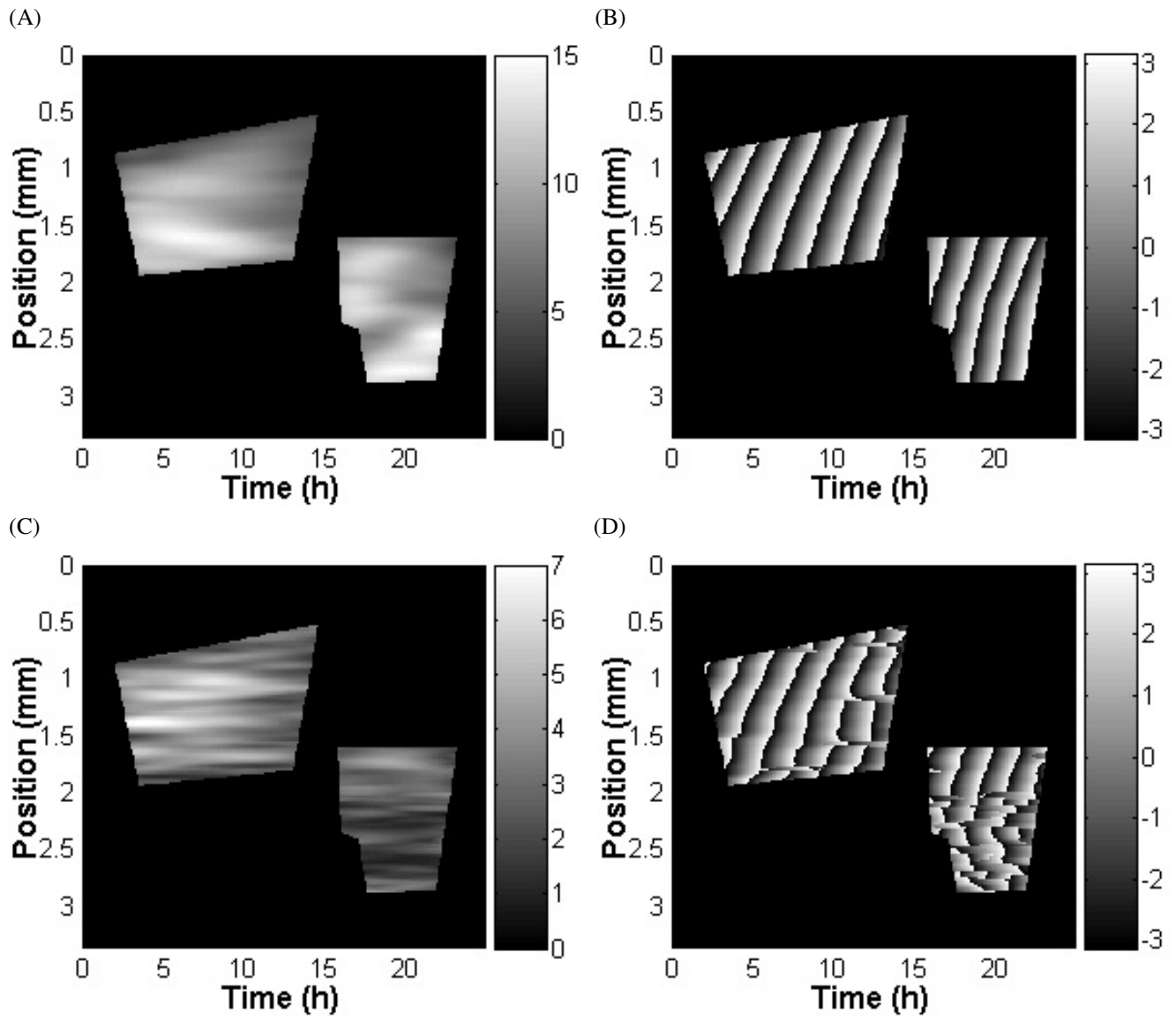
Supporting Figure S2. Large scale profiles. (A,B) Space-time diagram (kymograph) of $\bar{V}(x, t)$ (A) and $\bar{\rho}(x, t)$ (B). Space x is from top (0 mm) to bottom (3 mm), time t from left (0 h) to right (25 h), and the bottom-left region is the bare substrate in front of the monolayer. Color code \bar{V} from -0.15 (black) to $1.15 \mu\text{m}/\text{min}$ (green), $\bar{\rho}$ from $0.5 \cdot 10^{-3} \mu\text{m}^{-2}$ (black) to $3.5 \cdot 10^{-3} \mu\text{m}^{-2}$ (red). (C) Cell velocity \bar{V} vs cell density $\bar{\rho}$, same color code as Fig. 2A,B; $N = 319$ with mitomycin C, $N = 134$ in standard conditions. (D) Cell velocity \bar{V} vs mean effective cell radius R_{mean} , with a linear fit $\bar{V} = 0.1 R_{\text{mean}} - 0.8$; colors label the distance X to migrating front, from blue (500 μm or below) to red (2000 μm or above).



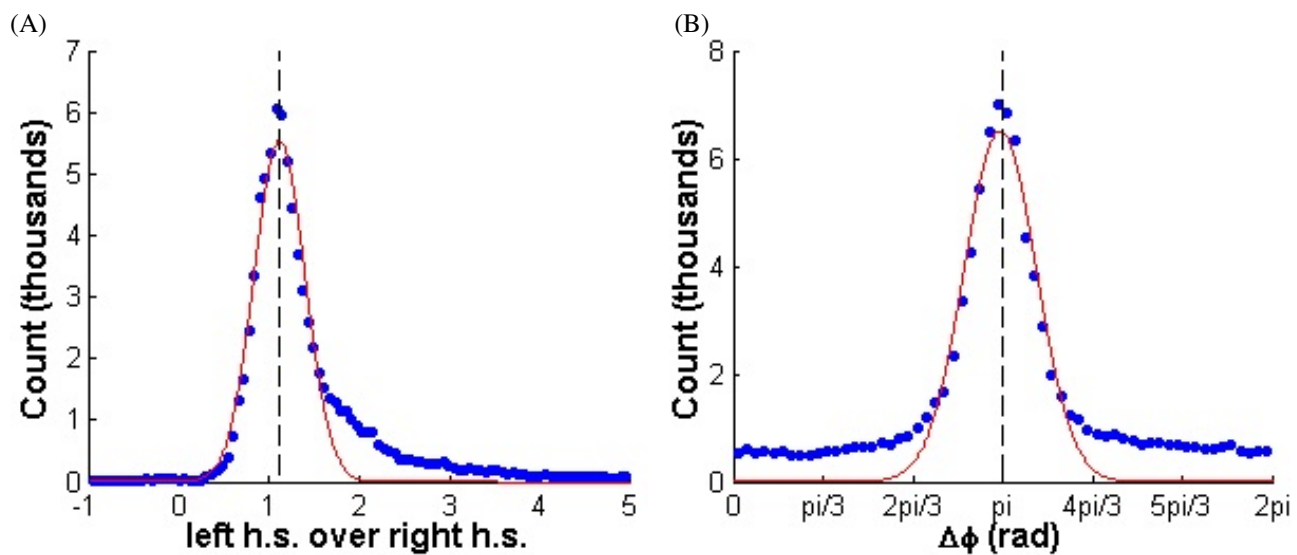
Supporting Figure S3. Small strip width. (A) Experiment performed with mitomycin C to prevent divisions. Bright-field images showing cell contours. (B) Corresponding kymograph of cell velocity V . (C,D) Same under standard conditions (i.e. without mitomycin C). In (A,C): Strip width $200\ \mu\text{m}$; migration from left to right; substrate: rigid PDMS. Despite the difference in the initial cell density, $10\ 10^{-3}\ \mu\text{m}^{-2}$ (A) vs $5\ 10^{-3}\ \mu\text{m}^{-2}$ (C), at the time the picture is taken ($t = 30\ \text{h}$) the density ranges in both experiments overlap. In (B,D): Color code V from -0.15 (black) to $1.15\ \mu\text{m}/\text{min}$ (green). Horizontal axis: time $t = 0$ (left) to $30\ \text{h}$ (right). Vertical axis: space $x = 0$ (top) to $3.8\ \text{mm}$ (B) or to $2.7\ \text{mm}$ (D).



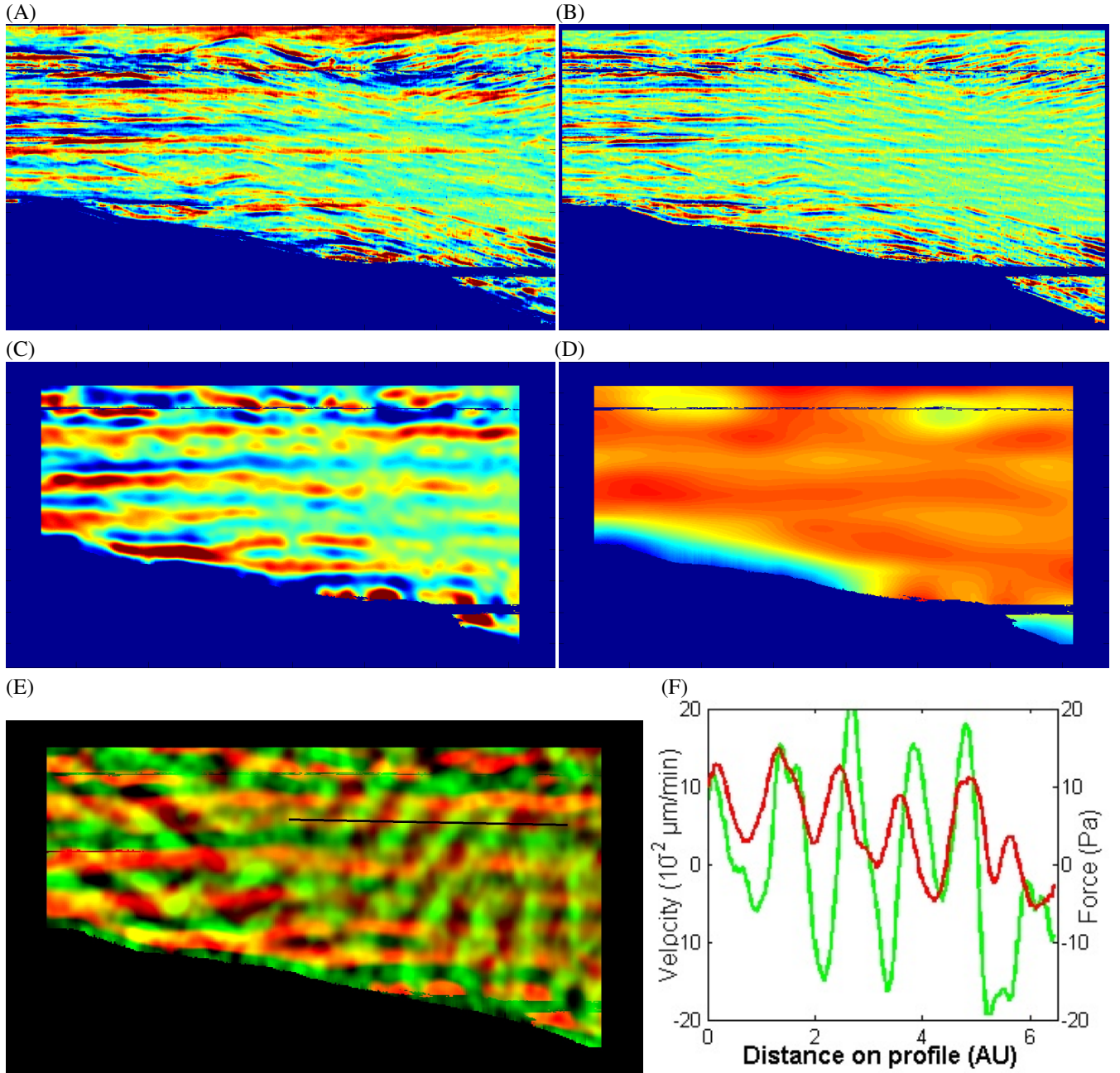
Supporting Figure S4. Local spatial variations. (A) Velocity $V(x, t)$ averaged over y but not over time; same representation as Fig. S2A,B. The outlined region of interest is selected manually as the region where waves have a good signal-to-noise ratio, large enough to perform the wavelet analysis of Fig. S5. (B) Histogram of relative amplitude of wave velocity cumulated for 8 different experiments. Red line: gaussian fit, of average 26.4% (marked by black dashes) and width 15.3% (C,D) Same for density. Gaussian fit: average 1.55 and width 0.83%.



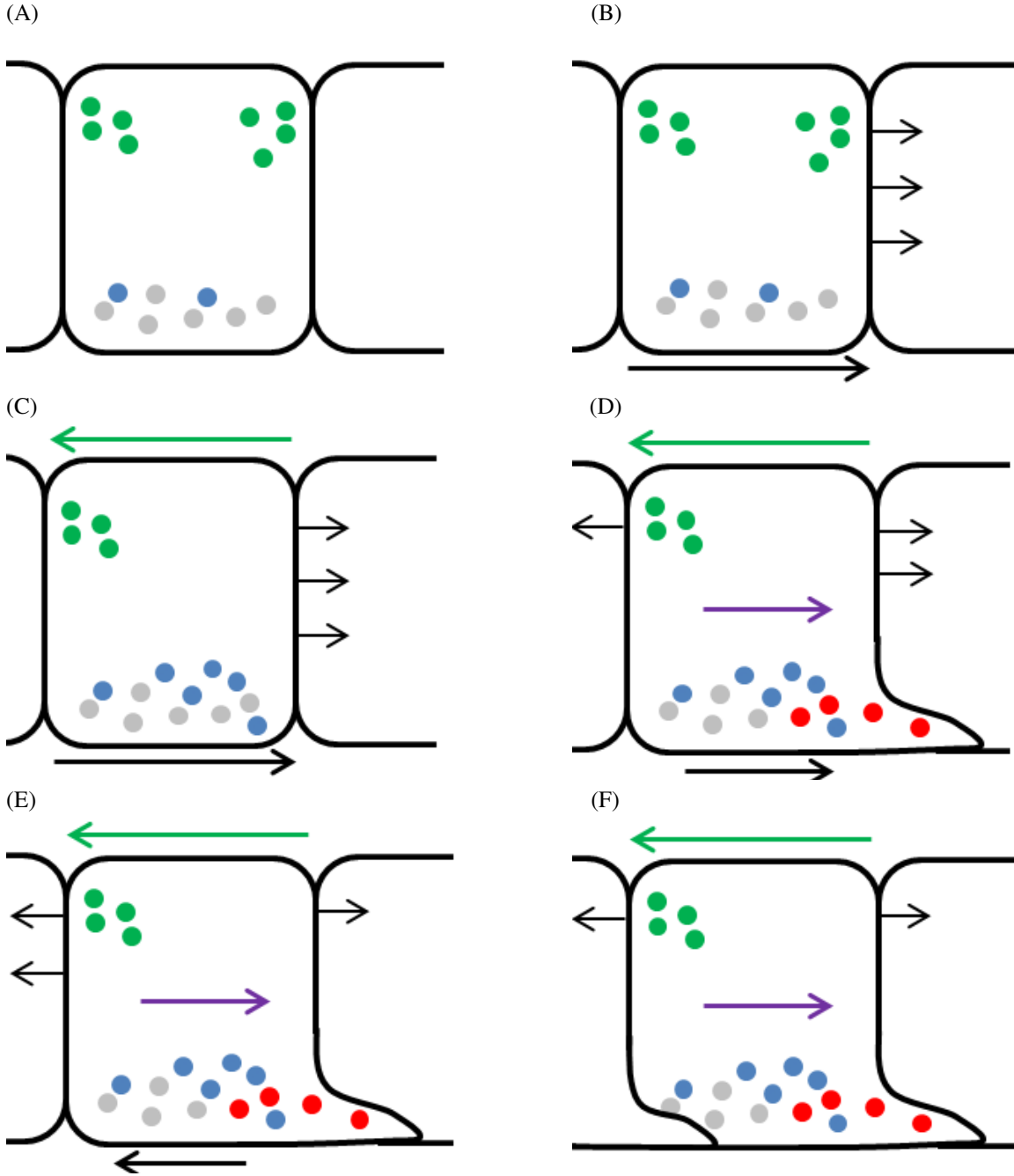
Supporting Figure S5. Example of local wave characteristics of velocity and density waves for a single experiment, determined by wavelet analysis in the region of interest (Fig. S4A). (A,B) Velocity wave: (A) amplitude $|\tilde{V}|$, in $10^{-2} \mu\text{m}/\text{min}$; and (B) phase ϕ_V , in rad. (C,D) Density wave: (C) amplitude $|\tilde{\rho}|$, in $10^{-5} \mu\text{m}^{-2}$; and (D) phase ϕ_ρ , in rad.



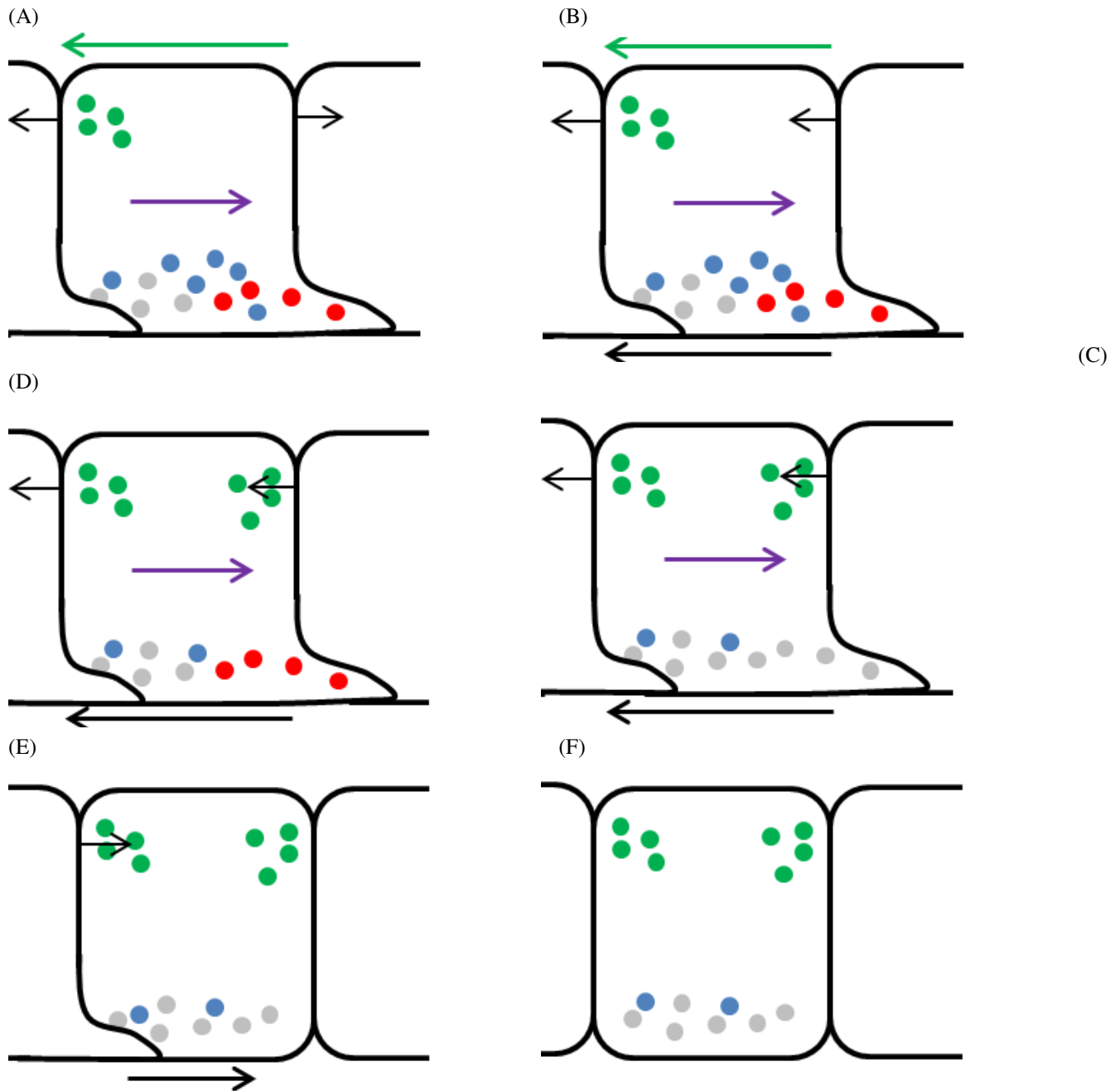
Supporting Figure S6. Test of equation for density, Eq. (2). (A) Histogram, cumulated for 8 different experiments, of the ratio of l.h.s., $|\hat{\rho}| (|c| + \bar{V})$ to r.h.s., $|\hat{\rho}| \bar{V}|$; red line : gaussian fit, of average 1.11 (vertical dashes). (B) Histogram of the difference $\phi_\rho - \phi_V$; red line : gaussian fit, of average 3.12 (vertical dashes).



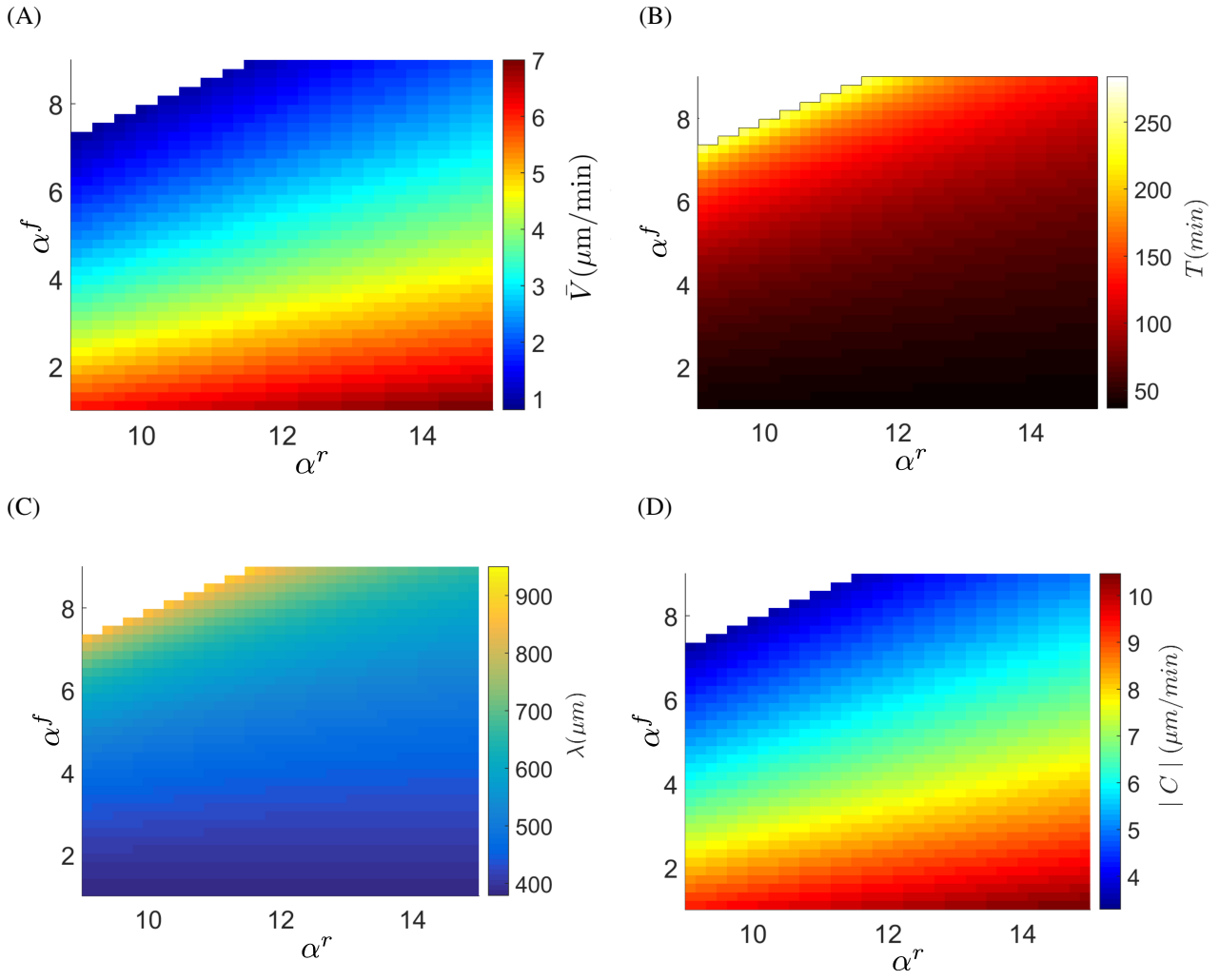
Supporting Figure S7. Example of force measurement. (A-D) Kymograph of force per unit area exerted by the cell monolayer on the substrate, $-F$: (A) raw measurement color code from -100 Pa (blue) to +100 Pa (red), and its decomposition into (B) small scales, from -100 Pa (blue) to +100 Pa (red), (C) middle scales, from -40 Pa (blue) to +40 Pa (red), and (D) large scales, from -120 Pa (blue) to +40 Pa (red). Space x is from top (0 mm) to bottom (2.8 mm), time t from left (0 h) to right (38 h), and the bottom-left region is the bare substrate in front of the monolayer. Horizontal blue bands reveal a lack of fluorescent beads. Bands advected at velocity V with the monolayer, which appear close to horizontal, correspond to inter-cell variability. Blue margins arise from sliding averages. (E-F) Test of equation for force, Eq. (6). (E) Merge of $-\tilde{F}$ (from (C)), from -20 Pa (black) to +20 Pa (red), and \tilde{V} , from $-0.2 \mu\text{m}\cdot\text{min}^{-1}$ (black) to $-0.2 \mu\text{m}\cdot\text{min}^{-1}$ (green). (F) Plot of $-\tilde{F}$ (red) and \tilde{V} (green) along the line manually drawn in (E).



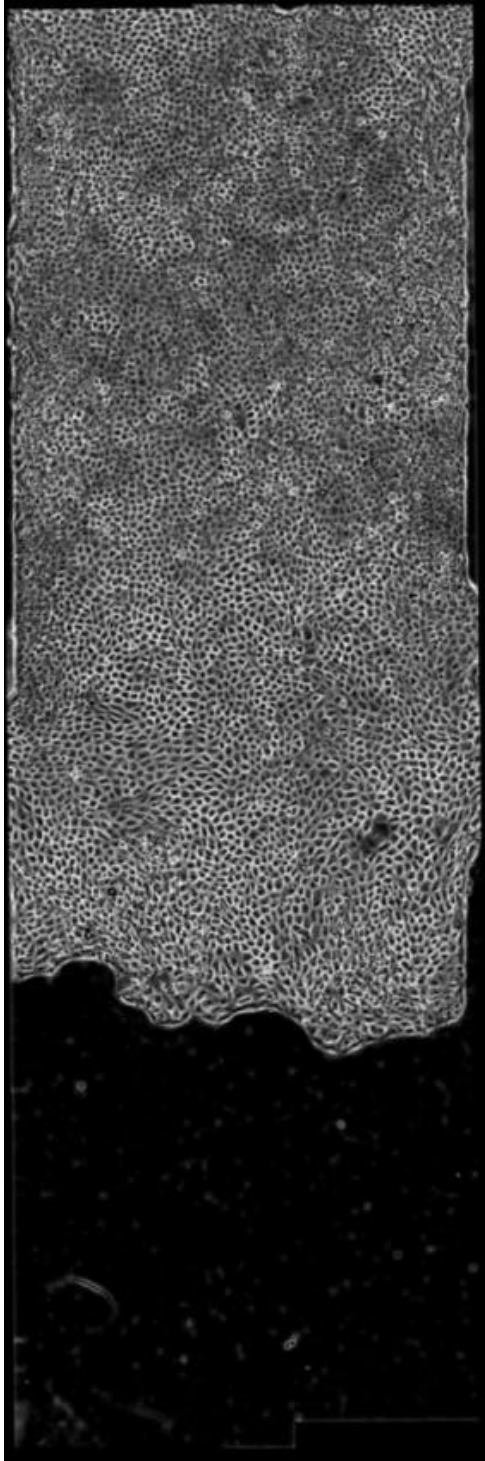
Supporting Figure S8. Propagation of migration in the bulk of the monolayer. A bulk cell is represented with part of its front neighbour (right) and rear neighbour (left). Points are proteins: Merlin at junctions (green) and in the cytoplasm (blue), Rac active (red) and inactive (gray). Arrows: left and right thin short arrows represent the forces exerted by neighbour cells; top green arrow is Merlin rear-front asymmetry $J^f - J^r$ pointing towards the left (rear) when $J^f - J^r > 0$; middle purple arrow is the cell velocity V ; bottom black arrow is the force resultant, or divergence of stress, $\partial\sigma/\partial x$. For legibility, we do not represent variations of cell length and height, nor the average stress. (A) The cell is initially at rest, Merlin is at junctions and Rac is inactive. (B) It is pulled by its front neighbour which migrates. (C) After ~ 10 min, this stretch relocates the front Merlin to the cytoplasm (Fig. 3i of Ref. (61)). (D) After ~ 20 more min, Rac activation on the front is observed, immediately followed by protrusive activity on the front and migration towards the front (Fig. 7h of Ref. (61)). (E) The cell pulls on its left neighbour, which is still immobile and resists. (F) The left neighbour migrates too, at the same velocity, and forces on the cell are balanced.



Supporting Figure S9. Propagation of migration arrest. Same symbols as Fig. S8. (A) The monolayer migrates as a whole, and forces on the cell are balanced (same picture as Fig. S8F). (B) The preceding cell (right neighbour) stops, and forces on the cell become imbalanced. (C) At the front junction, this induces Merlin relocalization at junction. (D) This inactivates Rac. (E) The cell retracts its protrusion and stops moving. This pushes on the rear neighbour (left) which still moves. (F) Equilibrium is reached when cells are at rest, Merlin is at junctions and Rac is inactive (same picture as Fig. S8A).



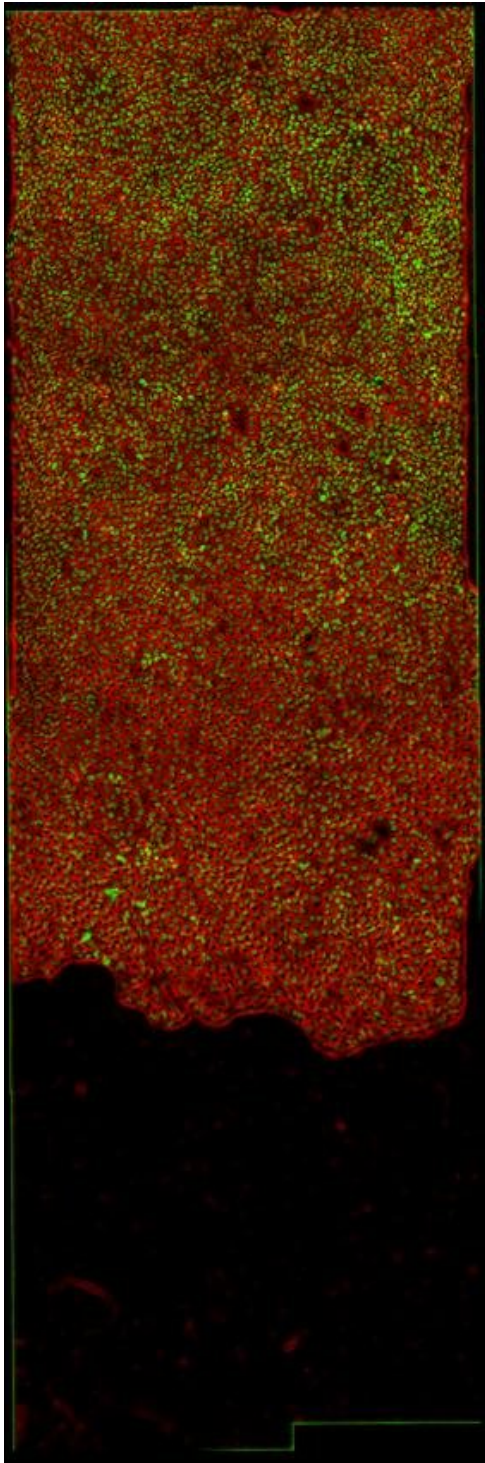
Supporting Figure S10. Model prediction for wave characteristics: (A) \bar{V} , (B) T , (C) λ , (D) $|C|$. The plots are calculated versus parameters α^f and α^r , using the values $D = 180 \mu\text{m}^2/\text{min}$ and $V_a = 9 \mu\text{m}/\text{min}$.



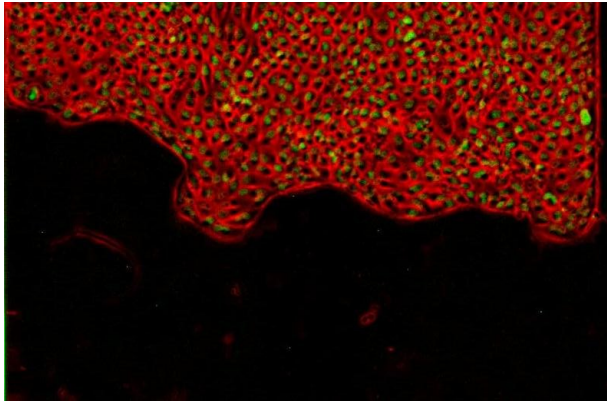
SI Movie 1. Monolayer of MDCK cells migrating within a straight strip with mitomycin C to prevent divisions. Bright-field image showing cell contours. Strip total length 4 mm, width 1 mm. The first image, noted $t = 0$, is taken after around 5 h of migration. Duration of the movie: 26 h. With respect to the original movie, the resolution has been decreased, and the time interval between frame has been doubled (10 min instead of 5 min).



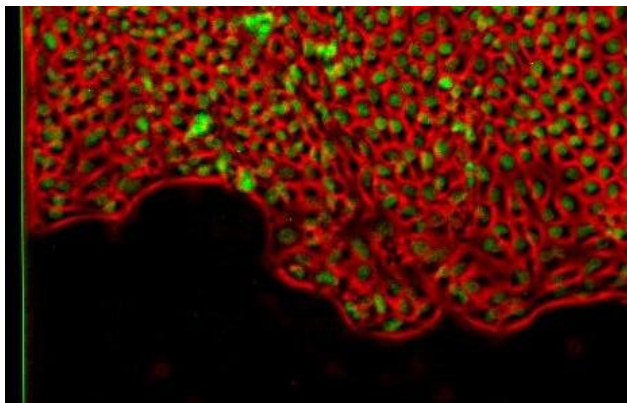
SI Movie 2. Same as SI Movie 1, nuclei labeled with histone GFP.



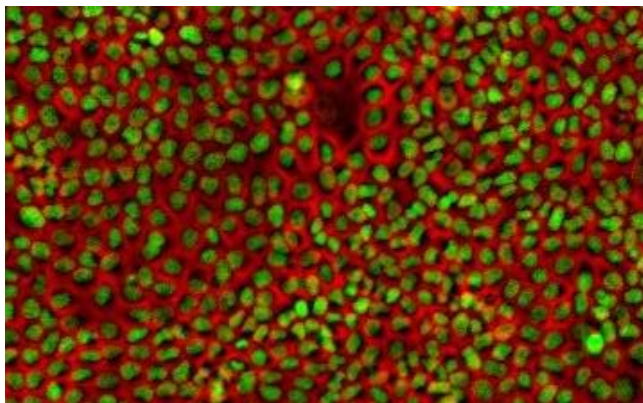
SI Movie 3. Merge of bright-field image showing cell contours (SI Movie 1) in red, and nuclei labeled with histone GFP (SI Movie 2) in green.



SI Movie 4. Same as SI Movie 3, with original time interval between frame (5 min), zoomed on the front.



SI Movie 5. Same as SI Movie 3, with original time interval between frame (5 min), zoomed on the middle.



SI Movie 6. Same as SI Movie 3, with original time interval between frame (5 min), zoomed on the back.